

Hubble Space Telescope Near-Infrared Snapshot Survey of 3CR radio source counterparts at low redshift¹

Juan P. Madrid², Marco Chiaberge^{2,3}, David Floyd², William B. Sparks²,
Duccio Macchetto^{2,4}, George K. Miley⁵, David Axon⁶, Alessandro Capetti⁷,
Christopher P. O’Dea⁶, Stefi Baum⁶, Eric Perlman⁹, Alice Quillen⁸

ABSTRACT

We present newly acquired images of the near-infrared counterpart of 3CR radio sources. All the sources were selected to have a redshift of less than 0.3 to allow us to obtain the highest spatial resolution. The observations were carried out as a snapshot program using the Near-Infrared Camera and Multiobject Spectrograph (NICMOS) onboard the Hubble Space Telescope (HST). In this paper we describe 69 radio galaxies observed for the first time with NICMOS during HST cycle 13. All the objects presented here are elliptical galaxies. However, each of them has unique characteristics such as close companions, dust lanes, unresolved nuclei, arc-like features, globular clusters and jets clearly visible from the images or with basic galaxy subtraction.

Subject headings: galaxies: elliptical and lenticular - galaxies: active - galaxies: jets - galaxies: surveys - infrared: galaxies

¹Based on observations made with the NASA/ESA Hubble Space Telescope, obtained at the Space Telescope Science Institute, which is operated by the Association of Universities for Research in Astronomy, Inc., under NASA contract NAS 5-26555. These observations are associated with program 10173.

²Space Telescope Science Institute, 3700 San Martin Drive, Baltimore, MD 21218.

³On leave from INAF, Istituto di Radioastronomia, Via P. Gobetti 101, Bologna, Italy, 40126-I.

⁴Affiliated with the Space Telescope Division of the European Space Agency, ESTEC, Noordwijk, The Netherlands.

⁵Leiden Observatory, P.O. Box 9513, NL-2300 RA Leiden, The Netherlands.

⁶Department of Physics, Rochester Institute of Technology, 85 Lomb Memorial Drive, Rochester, NY 14623.

⁷INAF - Osservatorio Astronomico di Torino, Strada Osservatorio 20, 10025 Pino Torinese, Italy.

⁸Department of Physics and Astronomy, University

1. Introduction

Extragalactic radio sources are often associated with massive elliptical galaxies. These so called radio galaxies are one of the most extraordinary astrophysical phenomena, powered, it is generally believed, by supermassive black holes in the galaxy nuclei. Radio galaxies are found in a variety of environments and across a wide range of redshifts.

The Revised Third Cambridge Catalogue (3CR) (Bennett 1962a, 1962b) is the best studied sample of radio loud galaxies and quasars. Spinrad et al. (1985) confirmed 298

of Rochester, Bausch & Lomb Hall, P.O. Box 270171, 600 Wilson Boulevard, Rochester, NY 14627.

⁹Joint Center for Astrophysics, Department of Physics, University of Maryland, Baltimore County, 1000 Hilltop Circle, Baltimore, MD 21250.

extragalactic radio sources of the 3CR catalogue. This catalogue was made based on the radio properties of the sources, and therefore its selection criteria are mostly independent with respect to orientation and HST wavelengths. The 3CR catalogue has, thus, excellent attributes for a survey.

Here we describe all the observations taken with our snapshot program in the HST Cycle 13. We are using NICMOS to obtain high spatial resolution, deep images in the near infrared H -band of 3CR sources at low redshift, $z < 0.3$. The primary goal of this project is to characterize the radio galaxy hosts free from the obscuring effects of dust, or at least, substantially reduced relative to the optical and UV. We also want to establish how radio galaxy hosts compare to the hosts of the most powerful high- z AGN, to QSO, and to quiescent ellipticals. The high linear resolution of HST grants us the possibility to observe details of the galaxies such as point-like nuclei, jets, and hot spots. These near-infrared observations are aimed at providing a zero redshift comparison sample for observations at high redshift.

This NICMOS snapshot program is a major enhancement to the dataset of HST observations of the 3CR sources. Successful snapshot programs have been carried out during past cycles in the optical and in the ultraviolet by Sparks and collaborators. The WFPC2 observations were presented by Martel et al. (1999) for $z < 0.1$, by de Koff et al. (1996) for $0.1 < z < 0.5$, and by McCarthy et al. (1997) for $z > 0.5$. UV observations with STIS were published by Allen et al. (2002). These successive HST programs have generated a database with a sample completeness comparable, for some range of redshift, to the radio catalogue. This database provides an excellent foundation for statistical studies as a vast number of observations of these sources are available for comparison at other wave-

lengths and with other instruments.

The content of this paper is as follows: Section 2 describes the observation strategy, Section 3 discusses the different steps of the data reduction, Section 4 highlights results obtained from this survey and gives near-infrared photometry, Section 5 presents three galaxies with jets visible with galaxy subtraction, in Section 6 we make comments on the image of each individual galaxy.

We use throughout this paper $H_0=71$ km.s⁻¹Mpc⁻¹, $\Omega_M = 0.27$, and $\Omega_\Lambda = 0.73$.

2. Sample selection and observations

There is a total of 115 objects in the 3CR catalogue with $z < 0.3$, 18 of them have been observed with NICMOS during previous cycles as part of other HST programs. We present 69 sources that have never been observed before, this corresponds to 71% of the sample. These new observations are associated with program 10173, PI: Sparks. This NICMOS survey uses snapshot exposures, a capability developed by the STScI to maximize the observing efficiency of HST. The observations obtained during this survey are taken at irregular intervals that fill the scheduling gaps between other accepted GO programs. The remaining 28 sources were not scheduled for observation during cycle 13. The observation log is presented in Table 1. Since the observed targets are randomly chosen based on the constraints of the observing schedule of HST, the 69 galaxies we present here are not biased towards any particular characteristic. Thus, they are suitable for statistical analysis.

The radio properties of the observed sample are given in Table 2. We present the flux density and radio power at 178 MHz, the radio spectral index, largest angular size, position angle, and Fanaroff and Riley (1974) morphological classification. The sources are

representative of large, steep spectrum, high power radio sources. The sources span three decades in radio power from $\log_{10} \sim 25$ to 28. The edge-darkened, lower luminosity FRI sources make up 26% of the sample.

All the observations presented here were carried out with NICMOS Camera 2 (NIC2) on MULTIACCUM observing mode. We use the MULTIACCUM sequence STEP32, which consists of rapid reads up to 32 seconds followed by 32 second steps. NIC2 has a field of view of $19.2'' \times 19.2''$ and a projected pixel size of $0.076'' \times 0.075''$. The measured FWHM for a bright source is $0.14''$.

The field size allows us to detect both the host galaxy and nuclear regions at the redshifts we aim. The coresponding physical scale over our redshift range varies from 0.335 kpc/arcsecond to 4.376 kpc/arcsecond.

We use the F160W filter, the analog of the *H* band. This filter is centered at $1.6037\mu\text{m}$, covering a wavelength range from $1.4\mu\text{m}$ to $1.8\mu\text{m}$, and includes the Paschen β emission line for objects at $z < 0.1$. For further details the reader is referred to the NICMOS Instrument Handbook (Noll et al. 2004).

All images have the same total exposure time of 1152 seconds, split into four exposures of 288s. We perform sub-pixel dithering to improve the PSF sampling and remove bad pixels. We use a squared dither pattern, with 7.4 pixels offsets.

3. Data processing

We obtain the data from the Multimission Archive at Space Telescope (MAST). The data are processed by the standard “on-the-fly” reprocessing calibration pipeline. The pipeline separates the data into science and engineering data, creates fits files and populates its headers. The pipeline also calibrates the raw data using CALNICA (Noll et al. 2004). We do the subsequent reduction of the data

with the NOAO image processing software Image Reduction Analysis Facility (IRAF).

The most important anomalies that we encounter in NIC2 images are: the pedestal effect, the amplifier glow, the coronagraphic spot, cosmic rays and bad pixels ¹. In this section we describe the steps we follow to get rid of these anomalies on the NICMOS images using different IRAF tasks.

NIC2 is divided into four quadrants of 128×128 pixels each. On visual inspection the raw images appear to have one quadrant darker than the others. This is particularly apparent for images with low background, e.g. small galaxies. This is known as the pedestal effect and is part of the instrumental signature for NICMOS. The origin of this effect is an additional offset introduced during the detector reset. The pedestal effect is stochastic and time variable, which makes it impossible to remove with the standard pipeline offered by the STScI (Noll et al. 2004).

We remove the pedestal effect with the tasks PEDSKY or PEDSUB from the NICMOS package under the HST calibration of the Space Telescope Science Data Analysis System (STSDAS).

These two tasks determine the pedestal offset of each quadrant with a similar technique. Both PEDSKY and PEDSUB assume that the image pixel value is the sum of the astronomical signal (source + sky), and the pedestal effect modulated by the flatfield. These tasks use the flatfield as input and loop over a range of trial values for the pedestal and find the best fit to the science image, for greater details see Bushouse et al. (2000).

PEDSKY does the fit of the pedestal only with those pixels near the background level. This task dismisses pixels containing signal from a source during the fitting process. PEDSKY removes the pedestal effect and also sub-

¹see also <http://www.stsci.edu/hst/nicmos/>

tracts the sky background. We use PEDSKY for galaxies that cover only a small fraction of the detector. This task is more effective when a large area of the image is free from sources in order to allow a better estimate of the background.

For sources covering a large portion of the detector we use the task PEDSUB to remove the pedestal effect. PEDSUB has a series of filters to remove unwanted features such as large galaxies. Contrary to PEDSKY, PEDSUB does not remove the background. In the case where the background is not removed, we use MSKY2, a task written by Mark Dickinson (private communication), that can fit the sky interactively, and subtract the sky mode from each image to obtain a zero level background.

Given the small projected size of the detector, a few galaxies cover the whole chip, for these images we adopt the median background of the other frames as the sky level. This is determined by measuring the sky level on 152 single exposures of the dither pattern. In these 152 exposures the source covers only a small fraction of the field of view. We find a median background of 0.046 counts per pixel with a standard deviation of 0.01806. For the galaxies covering most of the detector, the subtracted sky level amounts, on average, to 1.3% of the flux inside an aperture of 1kpc radius.

Some images have visible noise in the corners due to the amplifier glow of NIC2. This glow is caused by the readout amplifier situated close to each corner of the detector. Each time the detector is read out the amplifier warms up and emits infrared radiation that is detected by the chip (Noll et al. 2004). This anomaly does not affect the overall appearance of the image.

In order to obtain images of a better quality we create individual masks for each object to cover the small blemishes of the detector such as residual cosmic rays and bad pixels.

Furthermore, NIC2 has a hole through the camera to allow coronagraphic observations, which creates a circular spot on the images of about ten pixels in diameter. We treat this area with a mask to conceal the coronagraphic spot. We also create cosmic rays masks, with the task DRIZZLE_CR, that we incorporate into the individual masks for each object. The pixels of column 128 in NIC2 contains the first pixels read out in each quadrant and have an incorrect bias subtracted from them. This is called the "photometrically challenged" column. We applied a bad pixel mask to the pixels of this column. We recover, thus, information on the image.

The second extension of the NICMOS fits files contains the error image. We convert these error files into weightings which are the inverse square of the noise per pixel. The mask files are multiplied into the weight files described above, giving zero weight to bad pixels in the individual files but leaving the others unchanged.

We combine the four calibrated, background subtracted images of the dither pattern with the task DRIZZLE under the package DITHER (Fruchter & Hook 2002). The final weight files are called when dithering the four exposures of each object. The projected pixel size in the final image is $0.038''$.

DRIZZLE is also used to apply the necessary rotations to the images to obtain a north up, east left orientation. These final images are presented in Figures 1-77.

4. Analysis

4.1. Companions and morphology

The high spatial resolution provided by HST allows us to obtain images of the 3CR radio galaxies with unprecedented details.

All galaxies imaged during this program are ellipticals but each of them has its own peculiar characteristics and environment. In

our sample of 69 galaxies 36 of them (52%) have companions present in the field of view of NIC2. More than one third of this sample, i.e. 25 galaxies, have an unresolved nucleus and nine galaxies have dust lanes. Nineteen galaxies, primarily the closest, show off nuclear point-like sources likely to be globular clusters. Four galaxies have intriguing arc-like structures, which are perhaps lensed arcs or merger remnants.

4.2. Aperture photometry

We use the IRAF task RADPROF to measure the flux of the galaxies at five different radii. The radii of the apertures we use correspond to: 1 kpc, 5 kpc, 10 kpc, 15 kpc, 20 kpc. Given the small size of the detector we cannot always measure the flux at all five different radii.

The count rate (CR) is converted into flux using PHOTFLAM, the inverse sensitivity, in the header of the calibrated NICMOS images:

$$\text{PHOTFLAM}=1.74779.10^{-19} \text{ erg cm}^{-2} \text{ \AA DN}^{-1}$$

We determine the magnitudes in the Space Telescope (ST) system with the expression:

$$m_{ST} = -2.5 \log(\text{PHOTFLAM} \times \text{CR}) + \text{PHOTZPT}$$

where PHOTZPT is the ST magnitude zero point i.e. -21.1, see the HST Data Handbook for NICMOS (Dickinson et al. 2002). The limiting magnitude for the images presented here is about 25.3. We present the results of the near-infrared photometry in Table 3. Note that these magnitudes correspond to the total observed flux inside the radii set above. We did not perform photometry for the nuclei, which will be analyzed in detail in a forthcoming paper (Chiaberge et al. in preparation)

5. Ellipse residuals

We have used the ELLIPSE task in IRAF STSDAS.ANALYSIS.ISOPHOTE, based on the al-

gorithm of Jedrzejewski (1987), to fit elliptical isophotes to the NICMOS images. Each isophote is fitted at a pre-defined, fixed semi-major axis length. Starting from a first guess, the image is sampled along an elliptical path (defined by central coordinates (x_c, y_c) , position angle θ , and ellipticity b/a) to produce a 1-dimensional intensity distribution as a function of θ .

Modeling with ELLIPSE allows us to track radial changes in the ellipticity and position angle of the isophotes of galaxies. Models based on the best-fitting ellipse parameters are constructed in IRAF using the task BMODEL.

A complete sample of model-subtracted residual images of this survey will be presented by Floyd et al. (in preparation). Here we show two examples where jets are clearly visible with galaxy subtraction. This is the case for 3C66B, 3C133 Figures 10,23. Figure 62 shows the residual image for 3C401, its jet is also visible in the NICMOS image (Chiaberge et al. 2005).

6. Notes on individual sources

We provide here a short description of the most prominent features of the NICMOS images for each object.

3C20 The near-infrared image reveals a circular galaxy. One source is visible approx. $4.7''$ to the northwest of the nucleus. A bright unresolved source is present $5.2''$ to the southeast. This galaxy has a known radio hotspot detected by de Koff et al. (1996) with WFPC2. This hotspot falls outside the smaller field of view of NIC2.

3C28 3C28 is an elliptical elongated on the northwest to southeast direction. At least two other sources are present in the field of view: one is on the edge of

the chip to the northwest and the second one is $10.3''$ to the southwest. This galaxy is the cD of the X-ray cluster Abell 115 (McCarthy et al. 1995).

3C29 A round, undisturbed elliptical with a bright central unresolved component (nucleus). Several globular clusters are present in the field of view. This galaxy has a faint compact nucleus in the optical and in the UV. The UV nucleus was first detected by Allen et al. (2002).

3C31 This galaxy covers most of the area of the detector. A face on dust ring around the galaxy's nucleus can be seen on the infrared image. The WFPC2 image shows that this dust ring is composed of several dust strands with a larger absorption on the southwestern side (Martel et al. (1999) and de Koff et al. (2000)).

3C33.1 Elliptical galaxy with no obvious disturbance with an unresolved nucleus and a single close companion about $4''$ to the south-southwest. A bright unresolved source lies $12''$ to the southwest, three other faint unresolved sources are also visible as well as another double system $12''$ to the northwest.

3C35 This flattened galaxy is elongated northwest to southeast. The WFPC2 image of this galaxy shows an unremarkable elliptical (Martel et al. 1999) while the STIS image exhibits a faint compact nucleus (Allen et al. 2002).

3C52 The near-infrared image reveals an elongated galaxy in a crowded field. One unresolved source is present $6.5''$ to the northwest and a second unresolved source is located $9.7''$ to the north-northeast of the center of the galaxy. The near-infrared image does not show

the dust lane, perpendicular to the radio axis, visible in the optical (de Koff et al. (1996, 2000)).

3C61.1 The galaxy lies in the middle of the field of view which shows three prominent resolved companions. 3C61.1 is elliptical and compact. We do not see the tails of emission to the south and east detected by de Koff et al. (1996) with WFPC2. One unresolved source is present to the north of the galaxy.

3C66B This NICMOS image shows a round galaxy with a bright unresolved nucleus, several globular clusters and two unresolved sources to the south. We notice a small asymmetry in the shape of this galaxy with its northwest side more sharply defined than the southeast one. Zirbel & Baum (1998) claim that this slight asymmetry may be caused by a neighbor to the southeast. The jet of 3C66B is clearly visible in this NICMOS image after basic galaxy subtraction as shown in section 5.

3C75N 3C75N is slightly elongated on the east-southeast to the west-northwest direction. This is the northern component of a system of two elliptical galaxies, the edge of the southern companion is visible at the bottom of the image. Some faint globular clusters are also seen.

3C76.1 3C76.1 is an elliptical with a very elongated galaxy to the north, it is unclear from this image if they are interacting or not.

3C79 A galaxy with elliptical morphology, elongated north-south. The image shows two companions: one bright unresolved source less than one arcsecond south of the nucleus, and the other one to the north. 3C79 shows a complex

morphology in the optical, with no compact nucleus (de Koff et al. 1996)

3C83.1 The near-infrared image shows an elliptical elongated north to south and covering most of the detector area. The image reveals a thin dust lane wrapping around the nucleus. A bright nearby star generates diffraction spikes crossing the detector. Some faint globular clusters are also visible.

3C88 Elliptical elongated northwest to southeast, the radio-axis is perpendicular to the elongation of the galaxy. Globular clusters are visible on the image and there is no sign of disturbance or merger.

3C105 Highly flattened elliptical, faintly disturbed. A faint unresolved source is visible $4''$ to the west-southwest off the nucleus.

3C111 This galaxy has a very bright nucleus with the host clearly visible. 3C111 is an elliptical elongated north to south.

3C123 This elliptical galaxy is a member of a cluster. At least three diffuse companions and two point-like sources are present in the field of view. The optical image of de Koff et al. (1996) shows also a faint diffuse source.

3C129 An elongated arc-shaped source is clearly visible $3.4''$ east of the nucleus of the galaxy. Globular clusters in this galaxy are also detected. Several unresolved foreground stars are present in the field of view.

3C129.1 This very round elliptical galaxy is found in a region of high foreground stellar density. It is the cD of the cluster 4U0446+44. Globular clusters are also possibly present in the image.

3C130 This radiogalaxy is a round elliptical without peculiarities. It covers a large portion of the detector and lies in a region of high foreground stellar density. Thus a large number of point sources are visible. Some of them may be globular clusters.

3C133 We have discovered a new optical-IR jet in 3C133, see Floyd et al. (2006) for further discussion. The jet and eastern hotspot are well resolved, and visible at both optical and IR wavelengths, in spite of the low galactic latitude. The infrared jet follows the morphology of the inner part of the radio jet, with three distinct, aligned, bright knots east of the unresolved nucleus. The host is a round elliptical.

3C135 This FR II radio galaxy is a cluster member (McCarthy et al. 1995) with a close companion to the southwest.

3C165 The near infrared image reveals an elliptical elongated north to south in a crowded field. A source is present approx $7''$ to the northeast. 3C165 is a cluster member.

3C171 This galaxy of slightly disturbed elliptical morphology has particularly strong extended emission line regions. These emission line regions are aligned with the radio emission (Heckman et al. 1984, Blundell 1996). The NICMOS image shows faint tails, most likely Pa β emission, to the east and west overlapping the optical emission line regions, see zoom image.

3C173.1 Slightly boxy elliptical with faint companion $3''$ south. An asymmetric, low surface brightness component, is visible to the northwest, perhaps evidence of recent merger activity. 3C173.1 is a member of a group.

- 3C180** Our NICMOS image shows a boxy giant elliptical. 3C180 is a member of a cluster according to McCarthy et al. (1995). Five unresolved sources are present in the field of view.
- 3C184.1** This galaxy is a cluster member with several faint companions. It is an elongated elliptical with noticeable disturbed isophotes. An arc-shaped structure is present $\sim 2''$ northeast of the unresolved nucleus.
- 3C192** This object appears as a round, undisturbed elliptical galaxy in the near-infrared, while it shows a compact core with diffuse emission structures in the UV (Allen et al. 2002). Several globular clusters are also detected.
- 3C196.1** The near-infrared image shows an elliptical galaxy elongated northeast to southwest, which is the same direction of the radio emission. The same morphology is seen in the optical (de Koff et al. 1996 and Baum et al. 1988). Five other sources populate the field of view.
- 3C197.1** This galaxy has a round, slightly disturbed morphology and an unresolved nucleus.
- 3C198** The NICMOS image shows an elongated elliptical galaxy with a bright unresolved nucleus. The circumnuclear compact sources seen in the UV image (Allen et al. 2002) do not appear in the near-infrared.
- 3C213.1** This radio galaxy has an extended area of emission to the southeast. The near-infrared counterpart of the northern radio hot spot is clearly visible. The southern hot spot is also visible but is much dimmer. The two hotspots are also present on the WFPC2 image (de Koff et al. 1996, de Vries et al. 1997).
- 3C219** A member of a cluster of galaxies, this source shows five different companions of different types and a bright unresolved nucleus. As noted by de Koff et al. (1996) 3C219 appears to be interacting with the large companion to the southeast, however, McLure et al. (1999) modeled the WFPC2 image and found no evidence of such interaction.
- 3C223** Our near infrared image shows an asymmetric galaxy, slightly elongated northeast to southwest.
- 3C223.1** The image shows a galaxy with a very elongated elliptical shape and a thin dust disk to the southeast, see zoom image with different intensity scale. The dust disk is best seen in the optical (de Koff et al. 2000). A tail of emission is present to the northeast.
- 3C227** This is a broad line radio galaxy. We can clearly see the host galaxy and its bright nucleus on this near-infrared image. Both the optical and UV images show a very bright unresolved nucleus (Martel et al. 1999, Allen et al. 2000). A close companion is also visible $5''$ southeast off the nucleus.
- 3C236** Elliptical elongated from the northeast to the southwest. A dust lane is notable on the WFPC2 images and was detected by Martel et al. (1999). The absorption map of de Koff et al. (2000) clearly shows this dust disk too. O’dea et al. (2001) found four very blue regions of star formation on the edge of the dust lane.
- 3C277.3** The host galaxy of Coma A is a round elliptical. A source elongated

northeast to southwest is present approximately $5.8''$ to the southeast. This source is the radio knot K1 as defined by Miley et al. (1981) and van Breugel et al. (1985). The knot is also visible in the optical (Capetti et al. 2000). An unresolved source, likely to be associated to knot K2, is visible $1.8''$ southwest of K1.

3C285 Irregular clumps of emission linked to star formation are detected in the ultraviolet image of this galaxy (Allen et al. 2002). The near-infrared image shows a flattened galaxy elongated southeast to northwest. The dust lane perpendicular to the elongation of the galaxy is visible in both the WFPC2 and NICMOS images. A faint arc-like source is present approx. $5.1''$ to the southeast, see zoom image.

3C287.1 This broad line radio galaxy has a bright unresolved nucleus with visible diffraction spikes, the host is an elongated elliptical. A companion is present $5.1''$ to the northeast.

3C288 An E0 elliptical galaxy with round isophotes, a faint unresolved nucleus, and two compact nearby companions. One more extended companion is visible to the west. Two fainter companions are also present, one to the northwest and the other one to the southwest.

3C303 This galaxy is characterized by a strong X-ray emission (Hardcastle & Worrall 1999) and has a bright unresolved nucleus in the near-infrared image. A companion is visible $5.6''$ northeast of the nucleus.

3C310 As noted by Martel et al. (1999) for the optical image, this galaxy is flattened east-west, on an almost perpendicular direction to the radio jet axis.

The edge of a companion to the east is visible on the corner of the chip. There is a bright foreground star to the south of the galaxy. Globular clusters and a faint diffuse companion $7''$ northwest of the nucleus are also seen.

3C314.1 The NICMOS image shows an elliptical galaxy elongated east-northeast to west-southwest. The isophotes are elongated in the near-infrared as well as in the optical (de Koff et al. 1996).

3C315 This is a very elongated galaxy associated to an “X”-shaped radio source. A faint arc like feature is visible at the southern end of the galaxy, see zoom image. 3C315 has a very round large companion galaxy to the south. A small faint source is visible to the southwest of the chip.

3C319 The host galaxy associated to 3C319 is close to the southwest edge of the image. It appears as a slightly elongated elliptical. Three companions are also visible in the image.

3C321 This galaxy shows a clearly visible dust lane on our near-infrared image. A companion in the process of merging (Roche & Eales, 2000) is located $3.5''$ to the northwest and is elongated towards the central source along the radio axis. Bright knots of emission are present along the northern border of the dust lane on the UV image (Allen et al. 2002).

3C346 The northwestern galaxy of the double system corresponds with the radio core and has a very bright nucleus. The radio jet of this galaxy bends at a very bright knot, unresolved in the NICMOS image. This knot is located $\sim 2.2''$ to the east of the nucleus. The jet and

its knots are visible in this near-infrared image and in the optical as well (de Koff et al. 1996). The main companion galaxy is highly asymmetric and possibly merging with 3C346. A galaxy, likely to be an edge-on spiral, is visible to the southwest of the image.

3C348 This source, also known as Hercules A, is a cluster cD galaxy. 3C348 is a double-galaxy system in the process of merging (Sadun & Hayes, 1993). The radio core coincides with the southeastern galaxy. This galaxy has faint dust rings around the core in this near-infrared image. These rings are discussed in detail by Baum et al. (1996) based on WFPC2 observations.

3C349 The NICMOS image shows a boxy, elongated, slightly asymmetric elliptical galaxy with an unresolved nucleus.

3C353 A round giant elliptical with no signs of disturbance. Martel et al. (1999) find very circular isophotes ($e \approx 0.04$) on the optical image. A few small sources, most likely globular clusters, are visible around this galaxy.

3C371 This object is often classified as a BL Lac in the literature. In our image it appears as a round and smooth galaxy with a very bright nucleus that causes marked diffraction spikes.

3C379.1 Slightly elongated elliptical galaxy. We notice a curious arc-like feature $5''$ to the west. This arc like feature might be a lensed arc or a merger remnant, see zoom image.

3C381 Smooth elliptical with a close projected companion galaxy to the east. Roche & Eales (2000), with a U-band image taken with the Wide Field Camera on the Isaac Newton Telescope, find

an apparent tidal distortion that confirms that the two galaxies are interacting. There is an additional faint unresolved source $\sim 2''$ south.

3C382 This galaxy has a very bright unresolved nucleus with marked diffraction spikes. This galaxy lies on a field populated by unresolved sources.

3C386 This elliptical galaxy fills a large portion of the detector. New spectroscopic evidence shows that what appears to be a bright nucleus is a star superimposed on the center of the galaxy (Marchesini et al. private communication; Chiaberge et al. 2002). Several point sources are discernible on the field of view, some of them are possibly globular clusters.

3C388 This is the cD galaxy of an Abell class 2 cluster (Prestage & Peacock 1988) with a close bright and round companion to the southwest. Two possible nearby companions are visible within the halo of the galaxy, about $1''$ north of the nucleus. These two possible companions were also detected by Martel et al. (1999) in their WFPC2 image. In the near-infrared, they appear unresolved.

3C390.3 The host galaxy of this BLRG is clearly visible in our NICMOS image. A faint arc-like component is visible $\sim 3''$ southeast of the nucleus.

3C401 This elliptical shows an unresolved nucleus. The image shows a faint jet about $6''$ southwest of the nucleus identified by Chiaberge et al. (2005) as the infrared counterpart of the brightest region of the radio jet. Chiaberge et al. find that the infrared emission dominates the spectral energy distribution of this jet. An elliptical companion

is visible $4''$ to the north. A bright unresolved source is present $7.5''$ north of the core. This object lies on the radio jet axis but is not associated with any of the radio features. In the optical image of de Koff et al. (1996) it appears as a diffuse source. It is possible that this object is an infrared-bright background galaxy.

3C402 A large, elongated, smooth elliptical with several point like sources which might be globular clusters.

3C403 Elliptical galaxy with a companion to the southeast. This galaxy appears to be in a region of high foreground stellar density.

3C430 A dust lane around the nucleus of this elongated elliptical is weakly visible on this image. Several foreground stars are present in the field of view. Some of this compact sources may be globular clusters.

3C433 This cluster member (McCarthy, 1995) has a peculiar radio jet oriented north-south. We see an elongated elliptical galaxy with a bright nucleus. The nucleus is totally absent in the optical band (Chiaberge et al. 1999). A patch of emission detected by de Koff et al. (1996) in the optical is also present to the northwest of the nucleus on our NICMOS image. Two companion galaxies lie to the north-northeast. A bright foreground star is visible on the northern corner of the image.

3C436 The galaxy has an elongated shape, somewhat aligned with the radio image. An elongated companion is present $8.7''$ to the east-northeast.

3C438 This cluster member has at least three companions, the brightest of

which lies approx. $4''$ to the northeast. This galaxy appears to be in a region of high foreground stellar density given the presence of eight unresolved sources on the HST image.

3C445 This BLRG appears as a round elliptical with a very bright unresolved nucleus and clearly visible diffraction spikes. Some faint globular clusters are also visible.

3C449 The NICMOS image of this galaxy shows the dust lane detected with WFPC2 by Martel et al. (1999) although with less dramatic features, see zoom image. The dust lane has been modeled as a warped disk by Tremblay et al. (2005). We also detect the abundant globular clusters seen in the optical. The galaxy is elongated north-south and occupies a large portion of the NIC2 chip.

3C452 An elliptical elongated east to west showing no signs of disturbance. A faint compact source is visible $1''$ southwest of the nucleus.

3C465 The NICMOS image shows an elongated galaxy with its close companion visible to the north. Globular clusters surround the galaxy. This galaxy, the brightest galaxy in the cluster Abell 2634, shows a faint unresolved nucleus from the near-infrared to the UV (Allen et al. 2002, Chiaberge et al. 1999) and a visible dust lane in the optical (Martel et al. 1999).

7. Conclusion

We have presented 69 HST NICMOS images of the near-infrared counterparts of radio sources of the 3CR catalogue at low redshift. These NICMOS images allow us to characterize

the host galaxies and their environment. We also detect special features such as jets, dust disks, nuclei, and hot spots. This database of high-quality near-infrared images presented in this paper provide an excellent foundation for future statistical studies of radio galaxies and galaxy evolution.

This research has made use of the NASA Astrophysics Data System Bibliographic services. This research also made use of the NASA/IPAC Extragalactic Database (NED) which is operated by the Jet Propulsion Laboratory, California Institute of Technology, under contract with the National Aeronautics and Space Administration. We are grateful to Eddie Bergeron and Santiago Arribas for helping us with the NICMOS data reduction.

REFERENCES

- Allen, M. G., et al. 2002, ApJS, 139, 411
- Baum, S. A., Heckman, T., Bridle, A., van Breugel, W., & Miley, G. 1988, ApJS, 68, 643
- Baum, S. A., O’Dea, C. P., de Koff, S., Sparks, W., Hayes, J. J. E., Livio, M., & Golombek, D. 1996, ApJ, 465, L5
- Bennett, A. S. 1962a, Mem. RAS, 68, 163
- Bennett, A.S. 1962b, MNRAS, 125, 75
- Blundell, K. M. 1996, MNRAS, 283, 538
- Bushouse, H., Dickinson, M., van der Marel, R. P. 2000, Astronomical Data Analysis Software and Systems IX, ASP conference series, Vol. 216 p. 531
- Capetti, A., de Ruiter, H.R., Fanti, R., Morganti, R., Parma, P., & Ulrich, M.-H. 2000, A&A, 362, 871
- Chiaberge, M., Capetti, A., Celotti, A. 1999, A&A, 349, 77
- Chiaberge, M., Capetti, A., Celotti, A. 2002, A&A, 394, 791
- Chiaberge, M., et al. 2005, ApJ, 629, 100
- de Koff, S., Baum, S. A., Sparks, W. B., Biretta, J., Golombek, D., Macchetto, F., McCarthy, P., & Miley, G. 1996, ApJS, 107, 621
- de Koff, S., et al. 2000, ApJS, 129, 33
- de Vries, W.H., et al. 1997, ApJS, 110, 191
- Dickinson, M.E., et al. 2002, HST NICMOS data handbook v5.0, ed. B. Mobasher, Baltimore, STScI
- Fanaroff, B. L. & Riley, J. M. 1974, MNRAS, 167, 31
- Floyd, D. J. E., et al. 2006, astro-ph/0602021
- Fruchter, A.S. & Hook, R. N. 2002, PASP, 114, 144
- Hardcastle, M.J. & Worrall, D.M. 1999, MNRAS, 309, 969
- Hardcastle, M.J. 2003, MNRAS, 339, 360
- Heckman, T. M., van Breugel, W. J. M., Miley, G. K. 1984, ApJ, 286, 509
- Jedrzejewski, R. 1987, MNRAS, 226, 747
- Martel, A., et al. 1999, ApJS, 122, 81
- McCarthy, P. J., Spinrad, H., van Breugel, W. 1995, ApJS, 99, 27
- McCarthy, P. J., Miley, G. K., de Koff, S., Baum, S. A., Sparks, W. B., Golombek, D., Biretta, J., & Macchetto, F. 1997, ApJS, 112, 415
- McLure, R.J., et al. 1999, MNRAS, 308, 377

- Miley, G. K., Heckman, T. M., Butcher, H. R.,
van Breugel, W. 1981, ApJ, 247, L5
- Noll, K., et al. 2004, NICMOS Instru-
ment Handbook”, Version 7.0, (Baltimore:
STScI)
- O’Dea, C.P., et al. 2001, AJ, 121,1915
- Prestage, R.M. & Peacock, J.A. 1988, MN-
RAS, 230, 131
- Roche, N., & Eales, S.A. 2000, MNRAS, 317,
120
- Sadun, A. C., & Hayes, J. J. E. 1993, PASP,
105, 379
- Spinrad, H., Djorgovski, S., Marr, J., &
Aguilar, L. 1985, PASP, 97, 932
- Tremblay, G. R. et al. 2005, astro-ph/0510650
- van Breugel, W., Miley, G., Heckman, T.,
Butcher, H., Bridle, A. 1985, ApJ, 290, 496
- Zirbel, E. L. & Baum, S.A. 1998, ApJS, 114,
177

TABLE 1
OBSERVATION LOG

Source (1)	Date (UT) (2)	α (3)	δ (4)	Gal Lat (5)
3C20	2005 Feb 27	00 43 09.27	+52 03 36.66	-10.79
3C28	2005 Jun 13	00 55 50.65	+26 24 36.93	-36.45
3C29	2004 Dec 4	00 57 34.88	-01 23 27.55	-64.22
3C31	2005 Jun 17	01 07 24.99	+32 24 45.02	-30.34
3C33.1	2004 Aug 15	01 09 44.27	+73 11 57.2	+10.38
3C35	2005 Mar 16	01 12 02.29	+49 28 35.33	-13.26
3C52	2005 Mar 11	01 48 28.90	+53 32 27.9	-8.38
3C61.1	2004 Aug 9	02 22 36.00	+86 19 08.0	+23.73
3C66B	2004 Nov 5	02 23 11.46	+42 59 31.34	-16.77
3C75N	2004 Nov 11	02 57 41.55	+06 01 36.58	-44.93
3C76.1	2005 Feb 6	03 03 15.0	+16 26 19.85	-35.96
3C79	2004 Oct 30	03 10 00.1	+17 05 58.91	-34.46
3C83.1	2005 Mar 12	03 18 15.8	+41 51 28.0	-13.13
3C88	2004 Nov 6	03 27 54.17	+02 33 41.82	-42.02
3C105	2004 Oct 26	04 07 16.46	+03 42 25.68	-33.62
3C111	2004 Dec 8	04 18 21.05	+38 01 35.77	-8.82
3C123	2004 Dec 7	04 37 04.4	+29 40 13.2	-11.66
3C129	2004 Dec 8	04 49 09.07	+45 00 39.0	+0.14
3C129.1	2004 Nov 22	04 50 06.7	+45 03 06.0	+0.30
3C130	2005 Apr 19	04 52 52.78	+52 04 47.53	+5.12
3C133	2004 Dec 13	05 02 58.4	+25 16 28.0	-9.91
3C135	2005 Apr 8	05 14 08.3	+00 56 32.0	-21.04
3C165	2005 Apr 26	06 43 06.6	+23 19 03.0	+8.67
3C171	2004 Nov 14	06 55 14.72	+54 08 58.27	+22.23
3C173.1	2004 Nov 22	07 09 24.34	+74 49 15.19	+27.27
3C180	2005 Feb 20	07 27 04.77	-02 04 30.97	+06.96
3C184.1	2004 Nov 26	07 43 01.28	+80 26 26.3	+28.86
3C192	2005 Jan 8	08 05 35.0	+24 09 50.0	+26.40
3C196.1	2005 Feb 1	08 15 27.73	-03 08 26.99	+17.07
3C197.1	2005 Apr 19	08 21 33.7	+47 02 37.0	+34.48
3C198	2005 May 3	08 22 31.9	+05 57 7.0	+22.95
3C213.1	2005 Feb 12	09 01 05.3	+29 01 46.0	+39.67
3C219	2004 Sep 14	09 21 8.64	+45 38 56.49	+44.76
3C223	2005 Feb 10	09 39 52.76	+35 53 59.12	+48.66
3C223.1	2005 Jan 18	09 41 24.04	+39 44 42.39	+48.92

TABLE 1—*Continued*

Source (1)	Date (UT) (2)	α (3)	δ (4)	Gal Lat (5)
3C227	2005 Mar 28	09 47 45.14	+07 25 20.33	+42.29
3C236	2004 Nov 2	10 06 01.7	+34 54 10.0	+53.98
3C277.3	2005 Mar 24	12 54 12.06	+27 37 32.66	+89.21
3C285	2004 Dec 5	13 21 17.8	+42 35 15.0	+73.39
3C287.1	2005 Jul 16	13 32 53.27	+02 00 44.73	+62.99
3C288	2004 Oct 31	13 38 50.0	+38 51 10.7	+74.66
3C303	2004 Dec 26	14 43 02.74	+52 01 37.5	+57.50
3C310	2004 Aug 13	15 04 57.18	+26 00 56.87	+60.21
3C314.1	2005 Feb 24	15 10 23.12	+70 45 53.4	+42.18
3C315	2004 Dec 30	15 13 40.0	+26 07 27.0	+58.30
3C319	2004 Dec 29	15 24 05.5	+54 28 14.6	+51.05
3C321	2004 Dec 27	15 31 43.4	+24 04 19.0	+53.88
3C346	2005 May 19	16 43 48.69	+17 15 48.09	+35.77
3C348	2005 May 9	16 51 08.16	+04 59 33.84	+28.95
3C349	2005 Mar 23	16 59 28.84	+47 02 56.8	+38.20
3C353	2004 Sep 9	17 20 28.16	-00 58 47.06	+19.65
3C371	2005 Jan 29	18 06 50.6	+69 49 28.0	+29.17
3C379.1	2004 Nov 5	18 24 32.53	+74 20 58.64	+27.85
3C381	2004 Nov 11	18 33 46.29	+47 27 02.9	+22.48
3C382	2005 Jun 22	18 35 03.45	+32 41 46.18	+17.45
3C386	2005 Jun 15	18 38 26.27	+17 11 49.57	+10.55
3C388	2004 Oct 19	18 44 02.4	+45 33 30.0	+20.22
3C390.3	2004 Sep 17	18 42 09.0	+79 46 17.0	+27.07
3C401	2004 Aug 11	19 40 25.14	+60 41 36.85	+17.77
3C402	2004 Dec 10	19 41 46.0	+50 35 44.9	+13.27
3C403	2004 Nov 6	19 52 15.81	+02 30 24.4	-12.31
3C430	2005 Jan 27	21 18 19.15	+60 48 06.88	+7.96
3C433	2004 Aug 18	21 23 44.6	+25 04 28.5	-17.69
3C436	2004 Nov 9	21 44 11.74	+28 10 18.67	-18.77
3C438	2004 Nov 18	21 55 52.3	+38 00 30.0	-12.98
3C445	2005 Jun 24	22 23 49.57	-02 06 13.08	-46.71
3C449	2004 Nov 11	22 31 20.63	+39 21 30.07	-15.92
3C452	2004 Nov 28	22 45 48.9	+39 41 14.47	-17.06
3C465	2004 Sep 28	23 38 29.41	+27 01 53.03	-33.07

NOTE.—Col. (1), 3CR number; col. (2) observation date; col. (3) right ascension for epoch 2000; col. (4) declination for epoch 2000; col. (5) galactic latitude.

TABLE 2
RADIO PROPERTIES OF THE NICMOS SNAPSHOT SURVEY

Source (1)	z (2)	S(178)(Jy) (3)	log ₁₀ P ₁₇₈ (4)	α (5)	LAS (6)	PA (7)	FR (8)
3C20	0.174	42.9	27.43	0.67	51	101	II
3C28	0.1952	16.3	27.11	1.06	30	166	II
3C29	0.04481	15.1	25.8	0.50	139	160	I
3C31	0.0167	16.8	25.0	0.57	1833	159	I
3C33.1	0.1809	13.0	26.95	0.62	216	45	II
3C35	0.0670	10.5	26.0	0.77	704	12	II
3C52	0.2854	13.5	27.37	0.62	51	20	II
3C61.1	0.184	31.2	27.35	0.77	186	2	II
3C66B	0.0215	24.6	25.4	0.62	330	54	I
3C75N	0.02315	25.8	25.5	0.71	692	111	I
3C76.1	0.0324	13.3	24.33	0.77	200		I
3C79	0.25595	30.5	27.63	0.92	86	105	II
3C83.1	0.0255	26.0	25.6	0.64	680	96	I
3C88	0.03022	15.3	25.5	0.52	259	60	II
3C105	0.089	17.8	25.74	0.58		335	II
3C111	0.0485	64.6	26.5	0.73	220	62	II
3C123	0.2177	189.0	28.28	0.70	23	115	II
3C129	0.0208	46.9	25.66	0.92			I
3C129.1	0.0222	10.5	25.07	0.89			I
3C130	0.1090	15.5	26.67	0.89			I
3C133	0.2775	22.3	27.57	0.70	12	107	II
3C135	0.1253	17.3	26.75	0.92	130		II
3C165	0.2957	13.5	27.41	0.71		159	
3C171	0.2384	19.5	27.37	0.87	30	100	II
3C173.1	0.2921	15.4	27.45	0.88	58	17	II
3C180	0.22	15.1	27.19	0.84		7	
3C184.1	0.1182	13.0	26.56	0.68	167	157	II
3C192	0.0598	23.0	25.10	0.79	200		II
3C196.1	0.198	18.6	27.18	1.16	4	43	II
3C197.1	0.1301	8.1	26.44	0.69	14	2	II
3C198	0.0815	9.7	26.1	0.69	338	38	II
3C213.1	0.194	6.6	26.71	0.55	43	162	II
3C219	0.1744	41.2	27.41	0.81	184	40	II
3C223	0.1368	14.7	26.75	0.74	300	164	II
3C223.1	0.107	6.0	26.14	0.56	117	15	II

TABLE 2—*Continued*

Source (1)	z (2)	S(178)(Jy) (3)	$\log_{10} P_{178}$ (4)	α (5)	LAS (6)	PA (7)	FR (8)
3C227	0.0861	30.4	26.7	0.67	246	86	II
3C236	0.10050	14.4	26.5	0.51	2514	122	II
3C277.3	0.0857	9.0	26.1	0.58	50	158	II
3C285	0.0794	11.3	25.46	0.95	184		II
3C287.1	0.2159	8.2	26.9	0.52	112	91	II
3C288	0.246	18.9	27.39	0.85	16	146	I
3C303	0.141	11.2	26.66	0.76	38	97	II
3C310	0.0535	55.1	26.5	0.92	323	165	I
3C314.1	0.1197	10.6	26.49	0.95	201	144	I
3C315	0.1083	17.8	26.62	0.72		11	I
3C319	0.192	15.3	27.07	0.90	93	49	II
3C321	0.096	13.5	26.4	0.60	309	121	II
3C346	0.161	10.9	26.76	0.52	13	71	II
3C348	0.154	351.0	28.23	1.00	191	101	I
3C349	0.205	13.3	27.07	0.74	82	142	II
3C353	0.03043	236.0	26.7	0.71	275	85	II
3C371	0.0500	3.7	25.3	0.30	277	59	II
3C379.1	0.256	7.4	27.01	0.68	76	161	II
3C381	0.1605	16.6	26.94	0.81	69	4	II
3C382	0.0578	19.9	26.2	0.59	179	50	II
3C386	0.0170	23.9	25.2	0.59	288	17	I
3C388	0.091	24.6	26.6	0.70	32	63	II
3C390.3	0.0561	47.5	26.5	0.75	231	145	II
3C401	0.20104	20.9	27.25	0.71	19	24	II
3C402	0.0239	10.1	25.1	0.56	528	163	II
3C403	0.0590	17.8	26.1	0.45	230	79	II
3C430	0.0541	33.7	26.3	0.72	99	35	II
3C433	0.1016	56.2	27.06	0.75	58	172	II
3C436	0.2145	17.8	27.23	0.86	105	173	II
3C438	0.290	44.7	27.91	0.88	19	136	I
3C445	0.0562	24.8	26.2	0.85	576	171	II
3C449	0.0171	11.5	24.9	0.58	1742	10	I
3C452	0.0811	54.4	26.9	0.78	277	79	II
3C465	0.0303	37.8	25.8	0.75	375	122	I

NOTE.—Col. (1), 3CR number; col. (2), redshift; col (3), radio flux density in Janskys at 178 MHz; col. (4), \log_{10} of the radio power at 178 MHz in W Hz^{-1} ; col. (5), radio spectral index determined between 178 and 408 MHz; col. (6), radio source largest angular size in arcseconds; col. (7), radio structure position angle measured north through east; col. (8), Fanaroff-Riley type.

References. — de Koff et al. (1996) and references therein, Martel et al. (1999) and references therein, Spinrad et al. (1985), updated values were taken from NED.

TABLE 3
HST NICMOS F160W PROPERTIES OF THE 3CR SNAPSHOT SURVEY

Source (1)	m_{1kpc} (2)	m_{5kpc} (3)	m_{10kpc} (4)	m_{15kpc} (5)	m_{20kpc} (6)	Comments (7)
3C20	20.606	19.270	19.016	18.883	18.733	Close companion
3C28	21.486	19.382	18.709	18.475	18.393	Close companion
3C29	17.966	15.741				Unresolved nucleus, globular clusters
3C31	14.795					Dust lane, globular clusters, unresolved nucleus
3C33.1	20.308	19.365	18.923	18.707	18.678	Close companion, unresolved nucleus
3C35	18.410	16.908	16.365			
3C52	21.348	19.436	19.006	18.842	18.779	Close companion
3C61.1	21.873	20.613	20.325	20.270		Close companion
3C66B	15.827					Globular clusters, unresolved nucleus, jet
3C75N	15.469					Close companion, globular clusters
3C76.1	17.038	15.995				Close companion, globular clusters
3C79	20.942	19.470	19.108	18.962	18.898	Close companion
3C83.1	15.457					Dust lane, globular clusters
3C88	17.212	15.545				Globular clusters
3C105	19.411	18.344	18.175			
3C111	17.053	16.572				Unresolved nucleus
3C123	21.694	19.851	19.337	19.117	19.010	Close companion
3C129	16.313					Globular clusters, arc?
3C129.1	16.561					Globular clusters
3C130	18.271	16.297	15.704	15.373		Globular clusters
3C133	20.754	19.868	19.593	19.447	19.323	Close companion, unresolved nucleus, jet
3C135	19.882	18.690	18.273	18.224		Close companion
3C165	21.910	20.187	19.722	19.595	19.556	Close companion
3C171	21.562	19.997	19.657	19.487	19.445	Close companion, emission line tails
3C173.1	21.119	19.425	18.998	18.837	18.759	Close companion
3C180	21.534	19.572	19.009	18.790	18.716	

TABLE 3—*Continued*

Source (1)	m_{1kpc} (2)	m_{5kpc} (3)	m_{10kpc} (4)	m_{15kpc} (5)	m_{20kpc} (6)	Comments (7)
3C184.1	19.261	18.432	18.284	18.275		Close companion, arc?, unresolved nucleus
3C192	17.988	16.942	16.893			Globular clusters
3C196.1	21.766	19.535	18.789	18.462	18.352	Close companion, globular clusters?
3C197.1	19.914	18.668	18.367	18.295		Unresolved nucleus
3C198	19.367	18.390	18.213			Unresolved nucleus
3C213.1	20.879	19.523	19.190	19.109	19.066	Hot spots
3C219	20.110	18.767	18.396	18.284	18.250	Close companion, unresolved nucleus
3C223	20.118	18.761	18.416	18.351		
3C223.1	18.841	17.660	17.386	17.327		Unresolved nucleus, dust lane
3C227	17.944	17.415	17.313	17.308		Close companion, unresolved nucleus
3C236	18.857	17.502	17.210	17.140		Dust lane
3C277.3	19.120	17.626	17.327	17.257		Close companion, radio knots
3C285	19.167	17.624	17.248	17.163		Dust lane, arc
3C287.1	19.731	18.971	18.717	18.626	18.576	Close companion, unresolved nucleus
3C288	22.113	19.476	18.657	18.367	18.227	Close companion, unresolved nucleus
3C303	19.230	18.243	17.961	17.868	17.854	Close companion, unresolved nucleus
3C310	18.483	17.120	16.927			Close companion, globular clusters
3C314.1	20.281	18.915	18.658	18.624	18.571	
3C315	19.363	18.424	18.185			Close companion
3C319	21.093					Close companion
3C321	19.047	17.266	16.597			Close companion, dust lane
3C346	20.162	19.060	18.345	18.019	17.932	Close companion, unresolved nucleus, jet
3C348	22.272	19.328	18.343	18.098	18.021	Close companion, dust lane
3C349	20.859	19.657	19.347	19.275	19.259	Unresolved nucleus
3C353	16.860	15.537				Globular clusters
3C371	16.007	15.555				Unresolved nucleus

TABLE 3—*Continued*

Source	m_{1kpc}	m_{5kpc}	m_{10kpc}	m_{15kpc}	m_{20kpc}	Comments
(1)	(2)	(3)	(4)	(5)	(6)	(7)
3C379.1	21.227	19.407	18.891	18.717		Arc
3C381	20.072	18.819	18.545	18.413	18.290	Close companion, unresolved nucleus
3C382	15.931	15.366	15.143			Unresolved nucleus
3C386	15.429					Globular clusters
3C388	19.534	17.101	16.337	15.884		Close companion
3C390.3	16.806	16.249	16.187			Unresolved nucleus, arc?
3C401	21.874	19.853	19.160	18.671	18.590	Close companion, unresolved nucleus, jet
3C402	15.915					Globular clusters
3C403	17.848	16.485				Close companion
3C430	17.653	16.400				Dust lane, globular clusters
3C433	18.922	17.500	17.057	16.615		Close companion, unresolved nucleus
3C436	20.920	19.217	18.780	18.614	18.585	Close companion
3C438	21.851	19.807	19.240	19.015	18.839	Close companion
3C445	16.802	16.499				Unresolved nucleus, globular clusters
3C449	15.418					Dust lane, globular clusters
3C452	18.564	17.191	16.643			
3C465	16.105					Close companion, globular clusters, unresolved nucleus

NOTE.—Col. (1), 3CR number; Col. (2) through (6) HST NICMOS F160W magnitude inside a circular aperture, centered on the nucleus, with a radius of 1, 5, 10, 15 and 20 kpc respectively; Col. (7) remarks on special features.

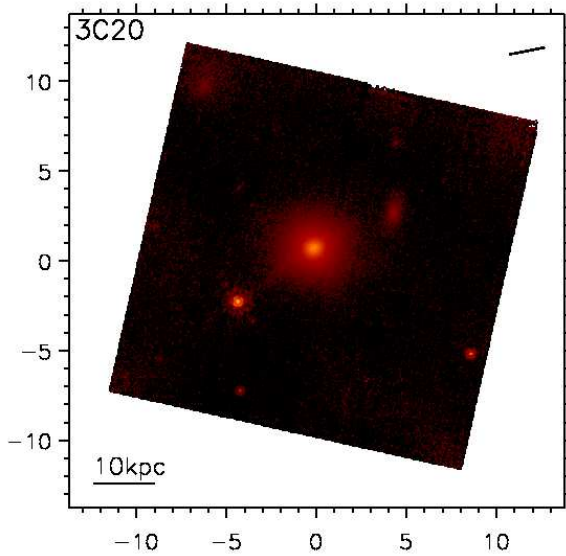


Fig. 1.— All images are rotated so they are north up and east left. Each figure is plotted within a box with vertical and horizontal axes in arcseconds. The intensity scale is logarithmic. A scale bar is plotted on the lower left corner in kpc, a second bar on the upper right corner of the image indicates the direction of the radio jet axis. This is HST/NICMOS F160W image of 3C20

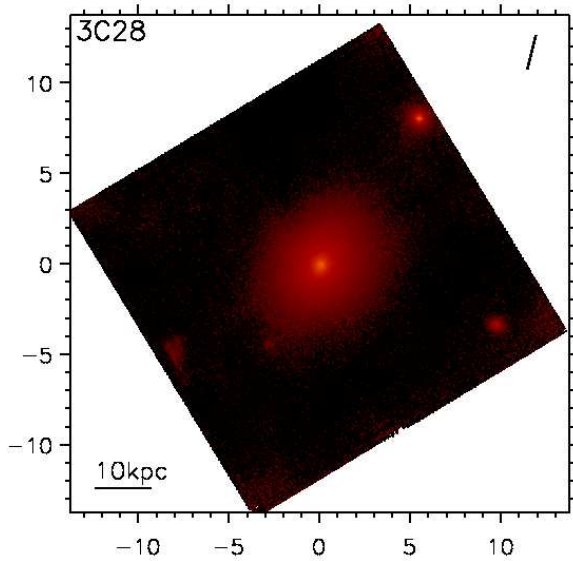


Fig. 2.— HST/NICMOS F160W image of 3C28

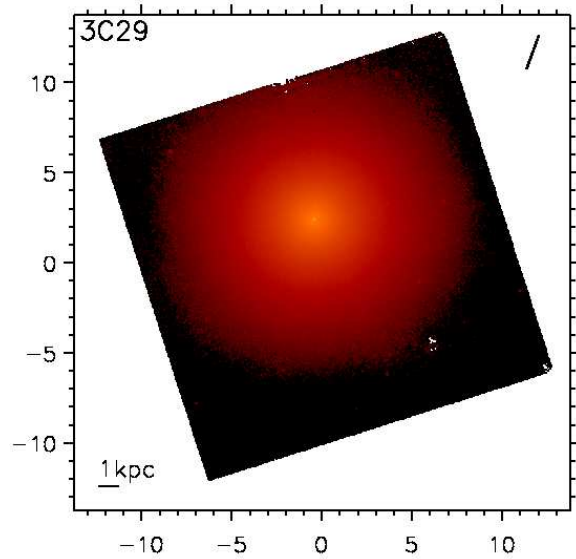


Fig. 3.— HST/NICMOS F160W image of 3C29

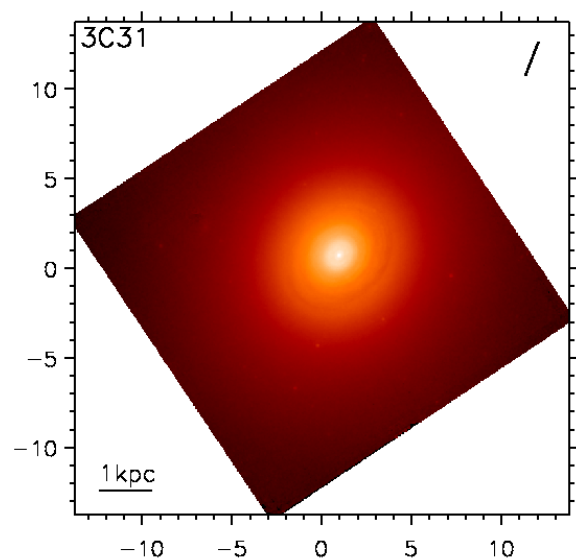


Fig. 4.— HST/NICMOS F160W image of 3C31

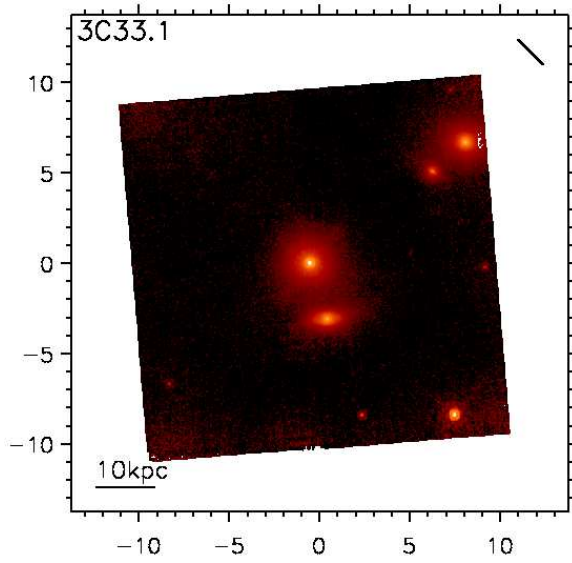


Fig. 5.— HST/NICMOS F160W image of 3C33.1

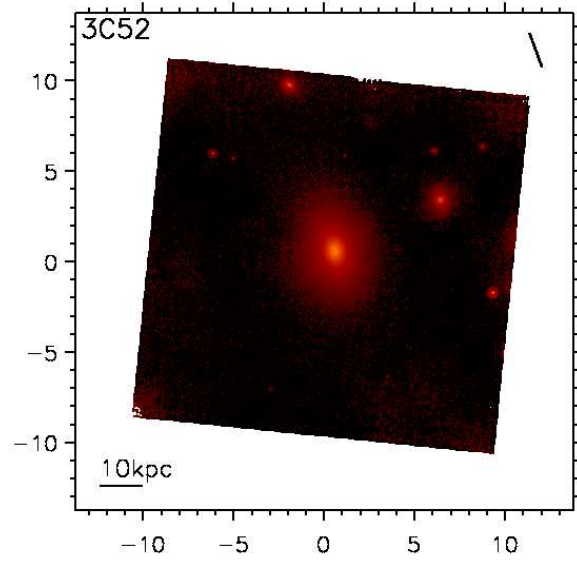


Fig. 7.— HST/NICMOS F160W image of 3C52

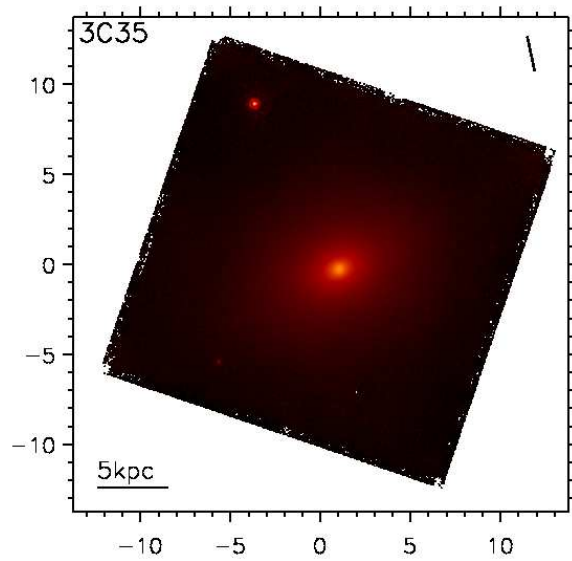


Fig. 6.— HST/NICMOS F160W image of 3C35

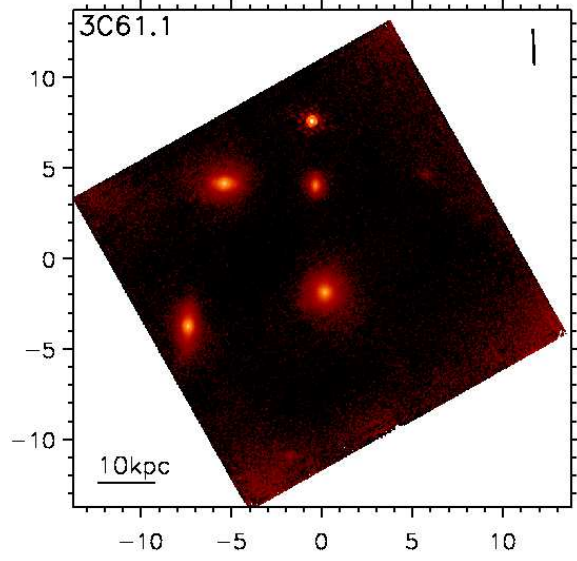


Fig. 8.— HST/NICMOS F160W image of 3C61.1

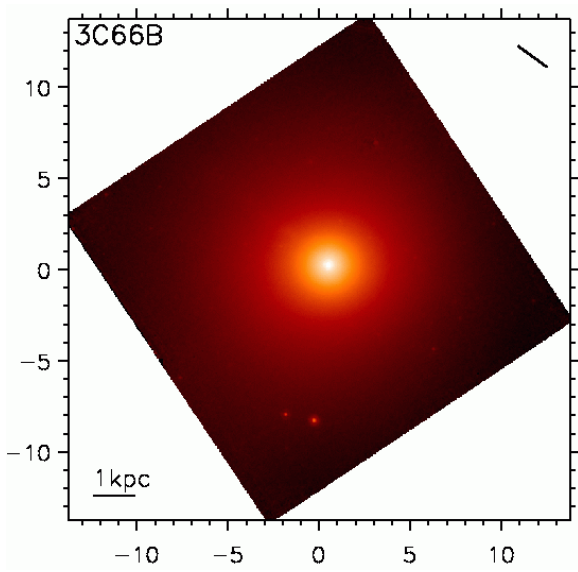


Fig. 9.— HST/NICMOS F160W image of 3C66B

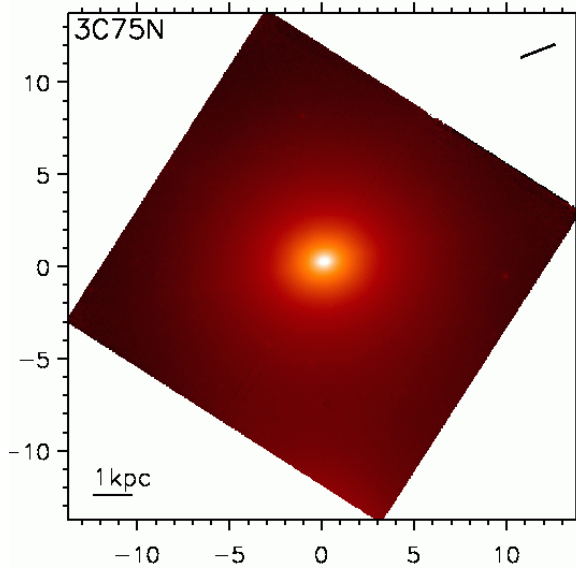


Fig. 11.— HST/NICMOS F160W image of 3C75N

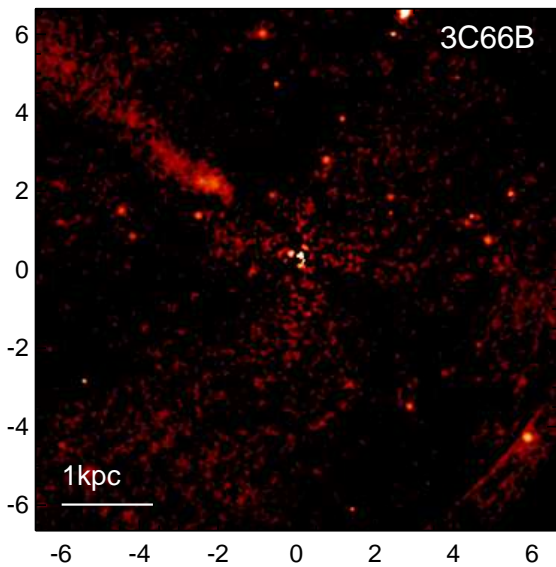


Fig. 10.— Model-subtracted residual for 3C66B

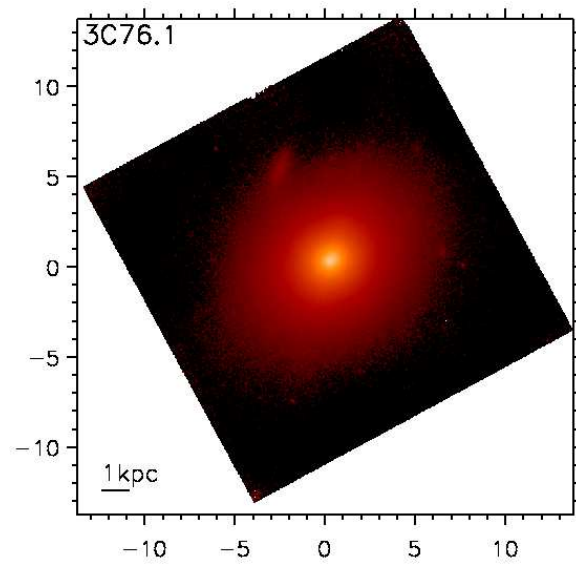


Fig. 12.— HST/NICMOS F160W image of 3C76.1

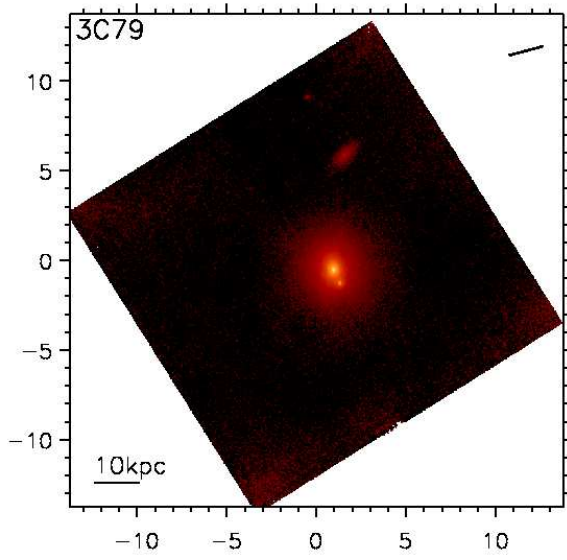


Fig. 13.— HST/NICMOS F160W image of 3C79

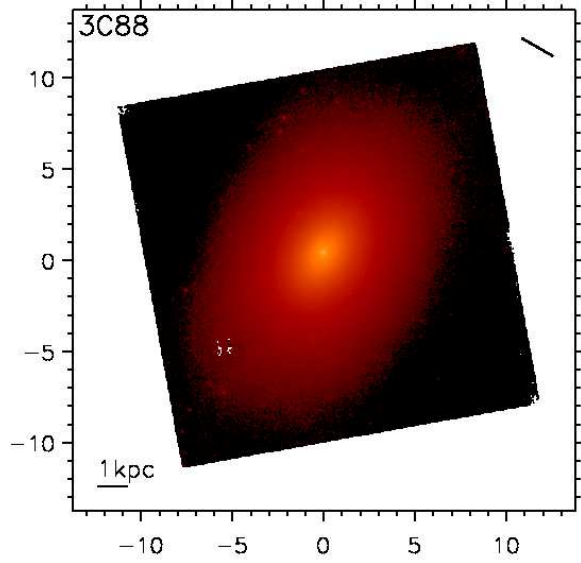


Fig. 15.— HST/NICMOS F160W image of 3C88

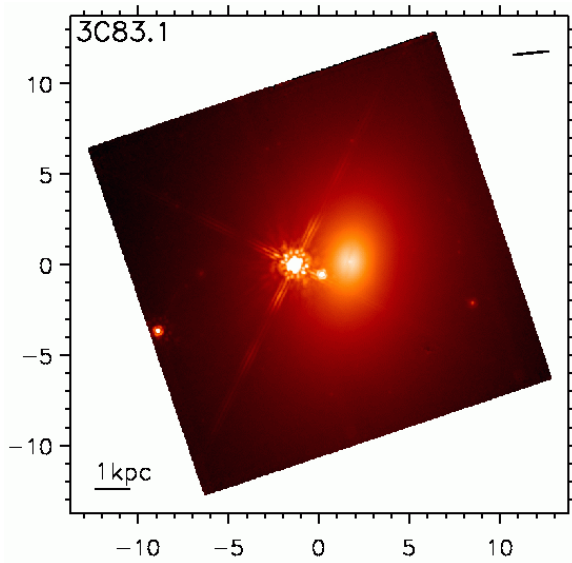


Fig. 14.— HST/NICMOS F160W image of 3C83.1

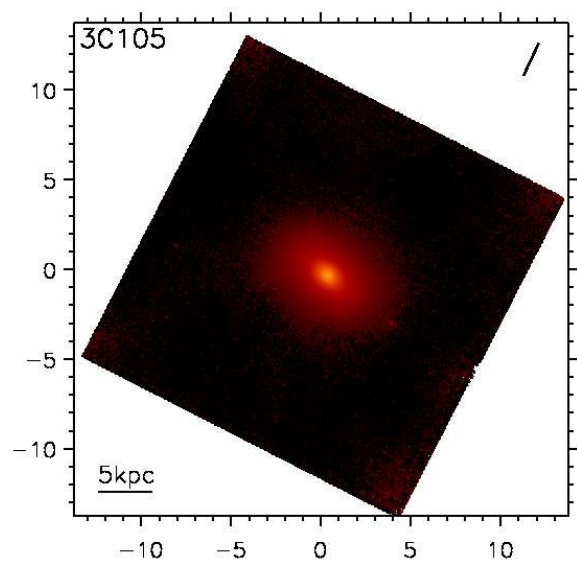


Fig. 16.— HST/NICMOS F160W image of 3C105

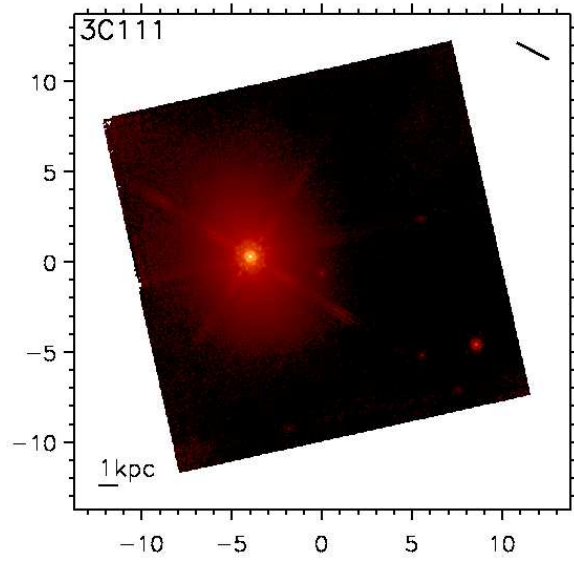


Fig. 17.— HST/NICMOS F160W image of 3C111

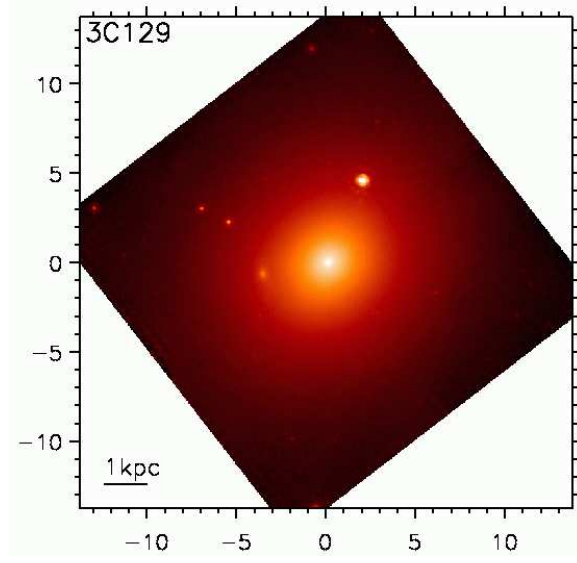


Fig. 19.— HST/NICMOS F160W image of 3C129

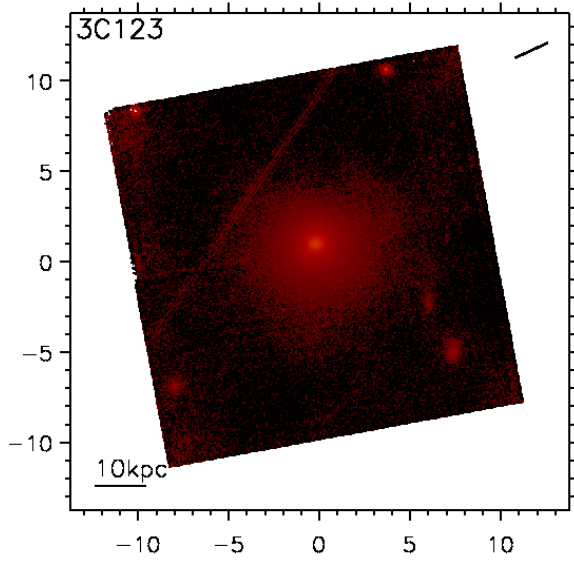


Fig. 18.— HST/NICMOS F160W image of 3C123

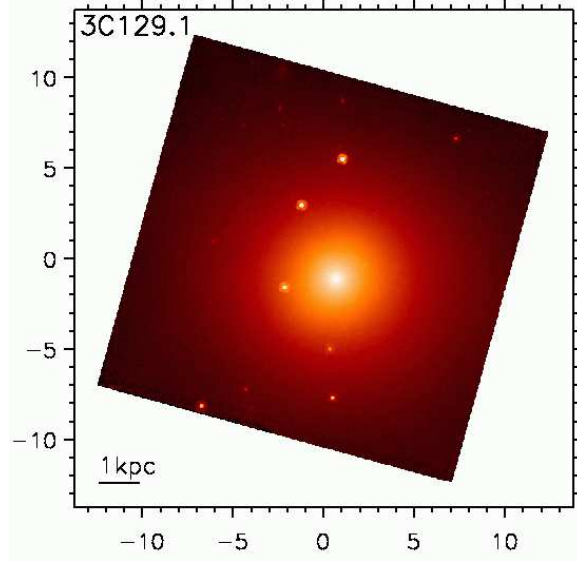


Fig. 20.— HST/NICMOS F160W image of 3C129.1

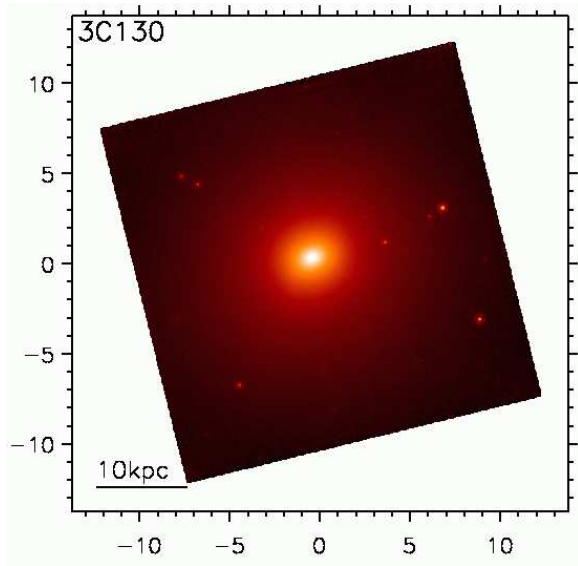


Fig. 21.— HST/NICMOS F160W image of 3C130

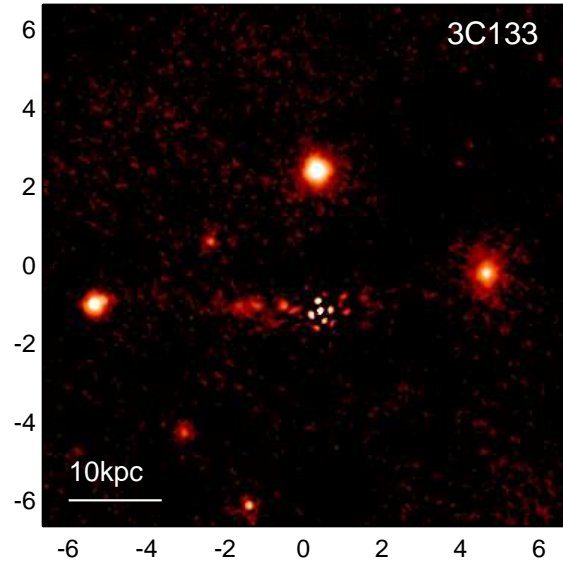


Fig. 23.— Model-subtracted residual for 3C133

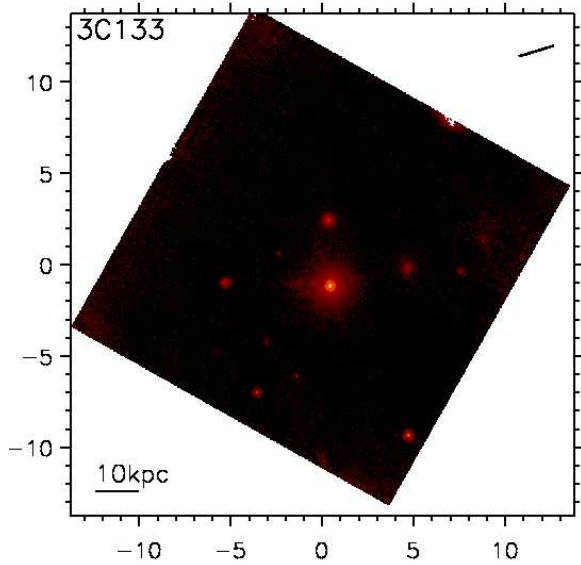


Fig. 22.— HST/NICMOS F160W image of 3C133

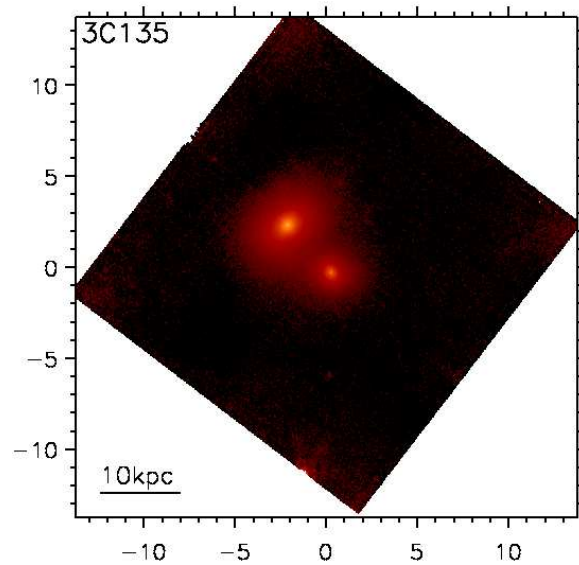


Fig. 24.— HST/NICMOS F160W image of 3C135

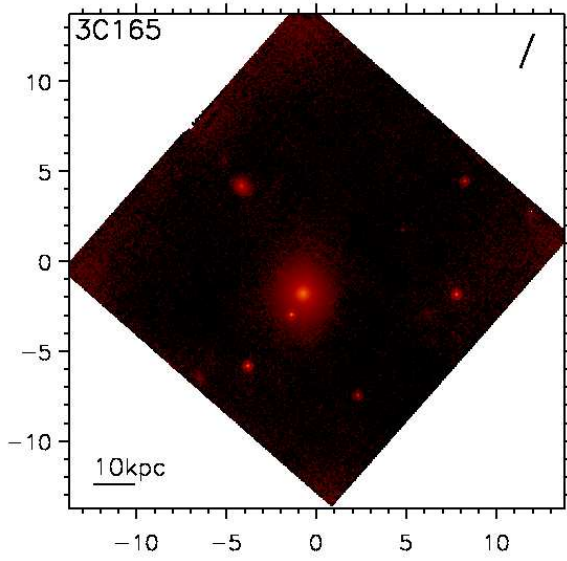


Fig. 25.— HST/NICMOS F160W image of 3C165

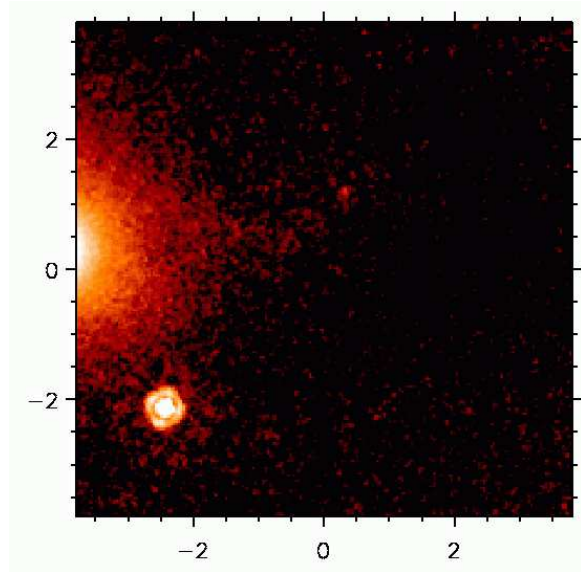


Fig. 27.— Zoom of a faint tail of emission to the west of the nucleus of 3C171

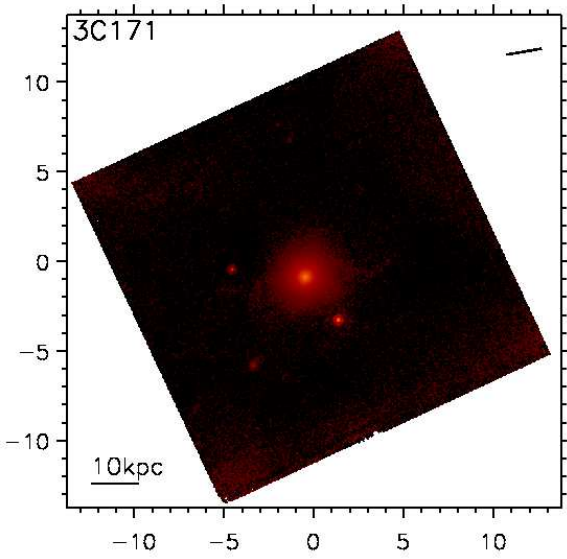


Fig. 26.— HST/NICMOS F160W image of 3C171

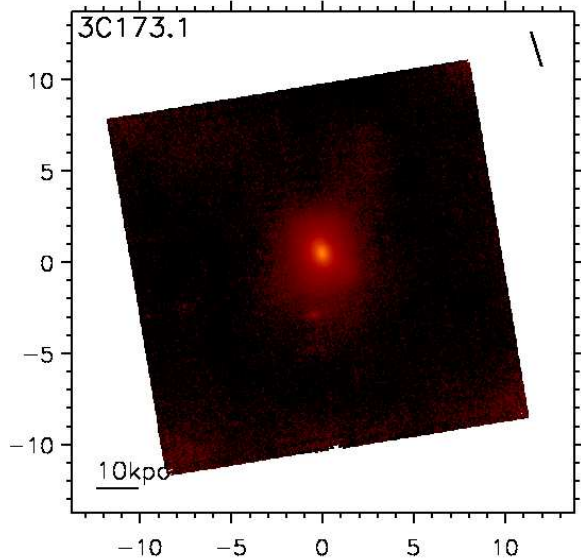


Fig. 28.— HST/NICMOS F160W image of 3C173.1

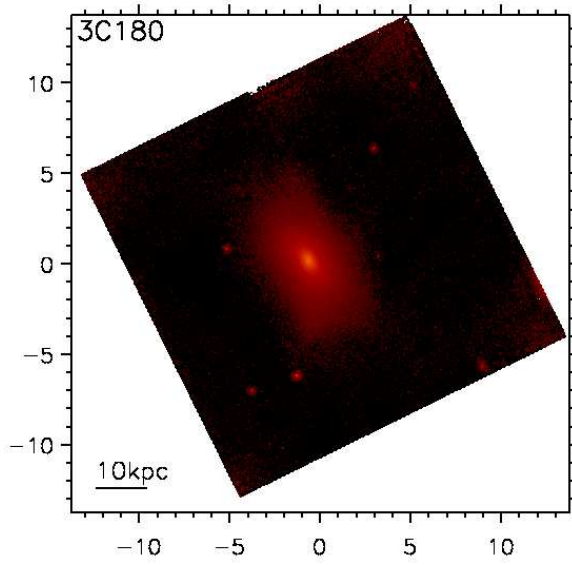


Fig. 29.— HST/NICMOS F160W image of 3C180

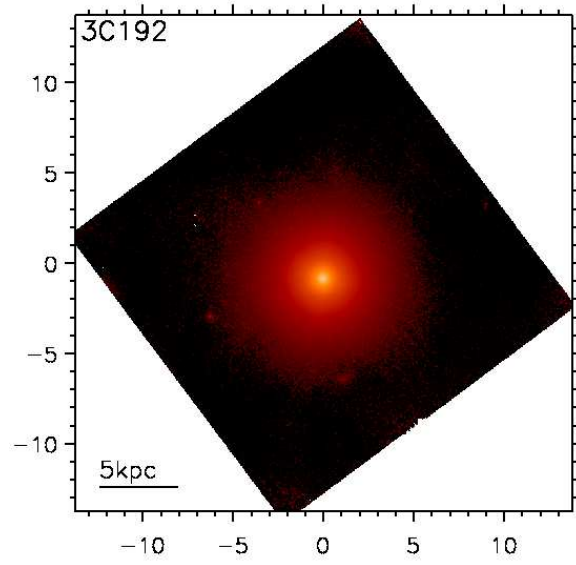


Fig. 31.— HST/NICMOS F160W image of 3C192

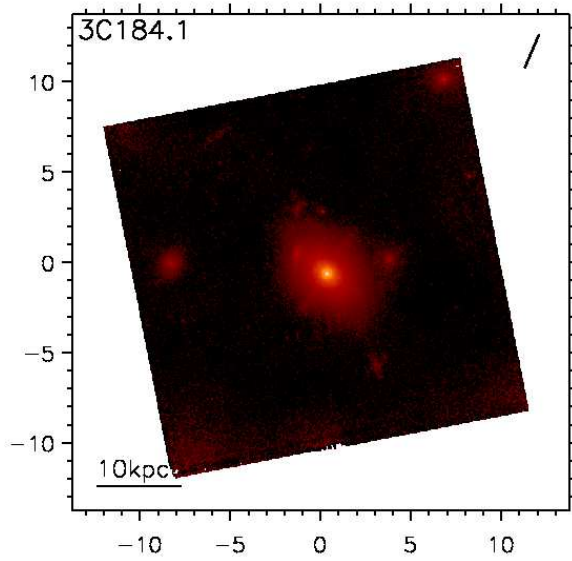


Fig. 30.— HST/NICMOS F160W image of 3C184.1

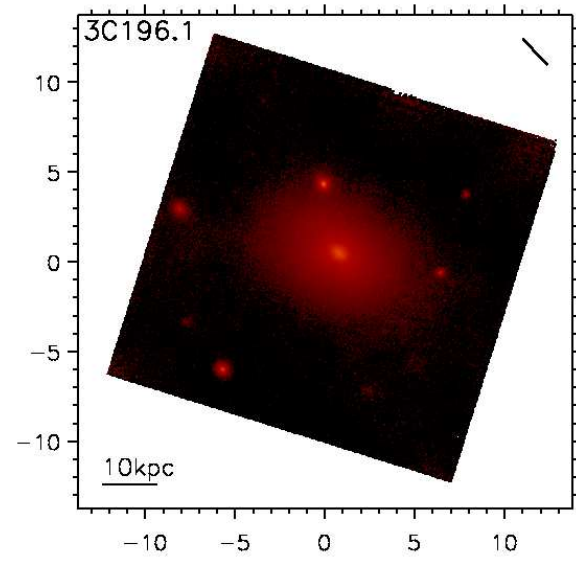


Fig. 32.— HST/NICMOS F160W image of 3C196.1

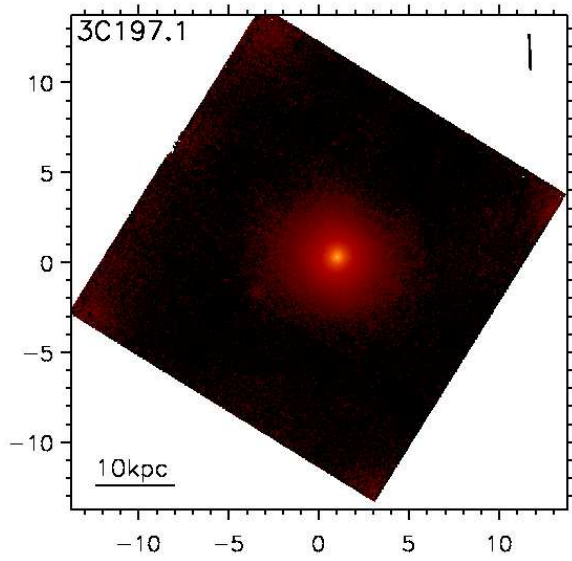


Fig. 33.— HST/NICMOS F160W image of 3C197.1

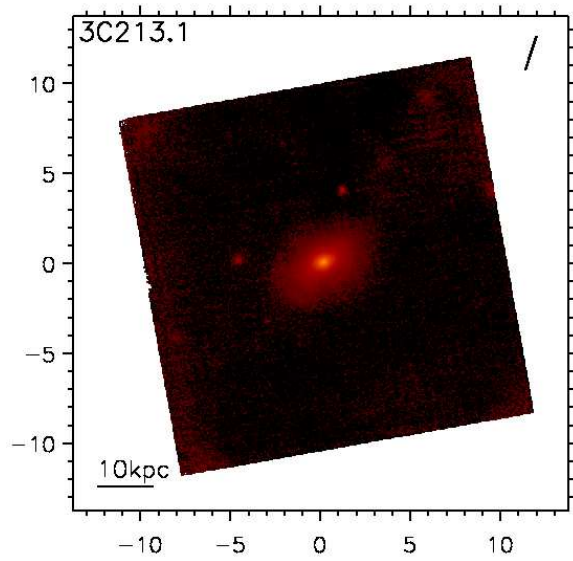


Fig. 35.— HST/NICMOS F160W image of 3C213.1

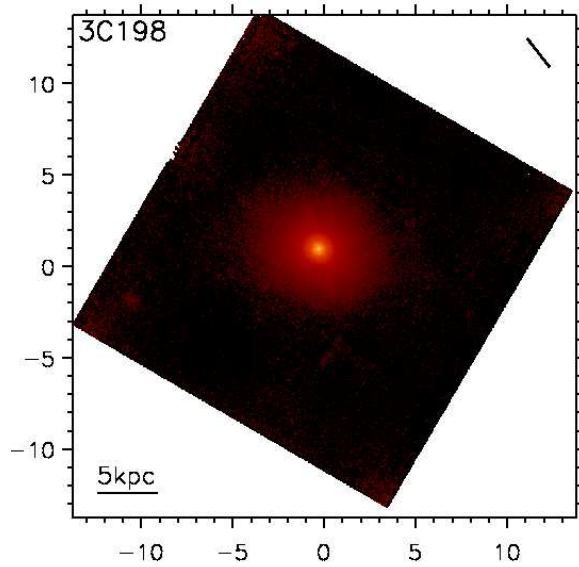


Fig. 34.— HST/NICMOS F160W image of 3C198

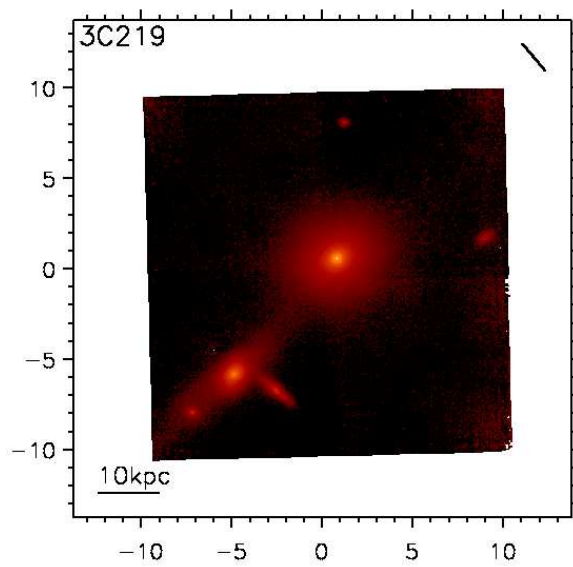


Fig. 36.— HST/NICMOS F160W image of 3C219

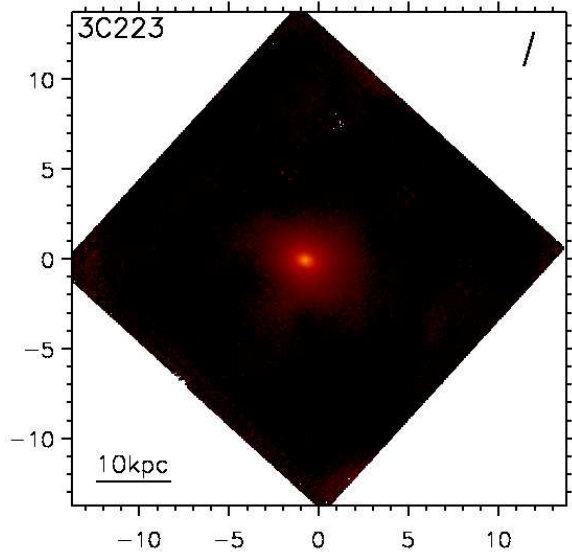


Fig. 37.— HST/NICMOS F160W image of 3C223

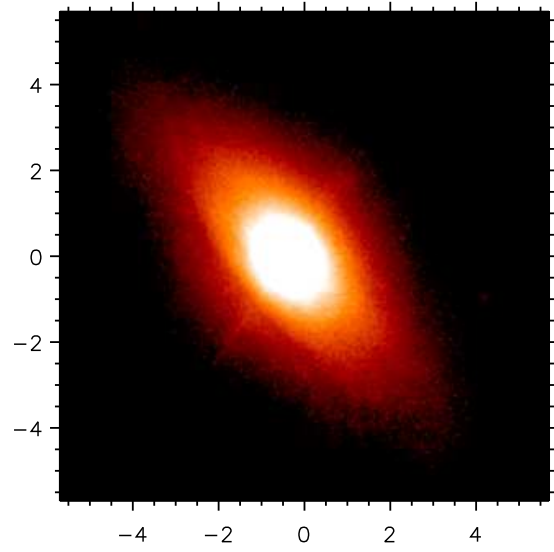


Fig. 39.— Thin dust disk to the southeast of 3C223.1

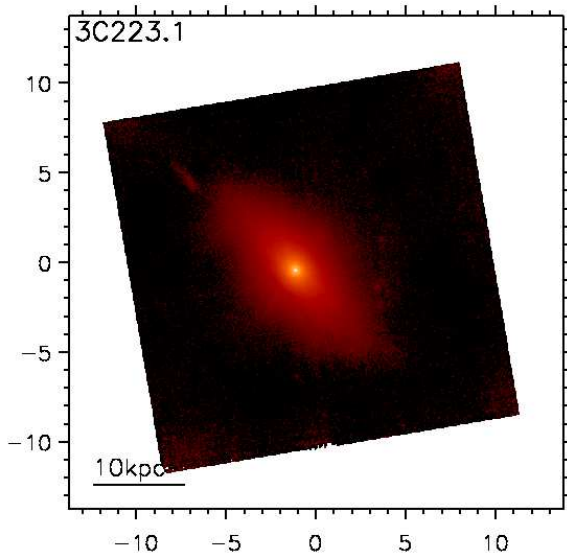


Fig. 38.— HST/NICMOS F160W image of 3C223.1

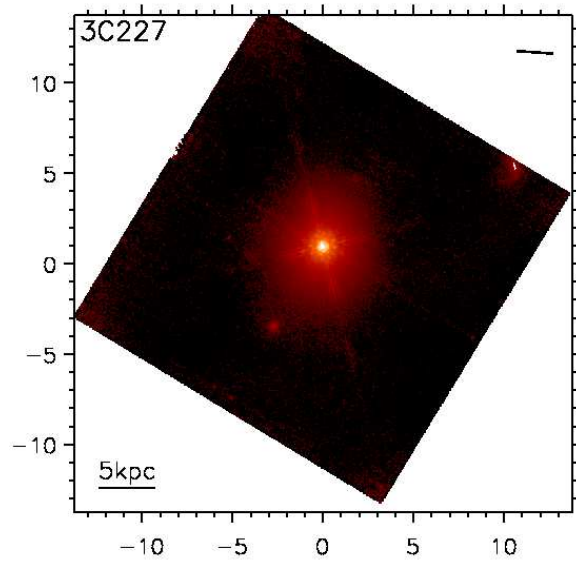


Fig. 40.— HST/NICMOS F160W image of 3C227

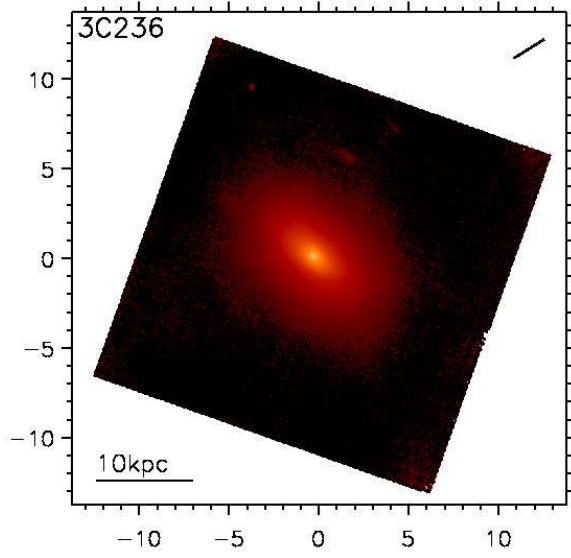


Fig. 41.— HST/NICMOS F160W image of 3C236

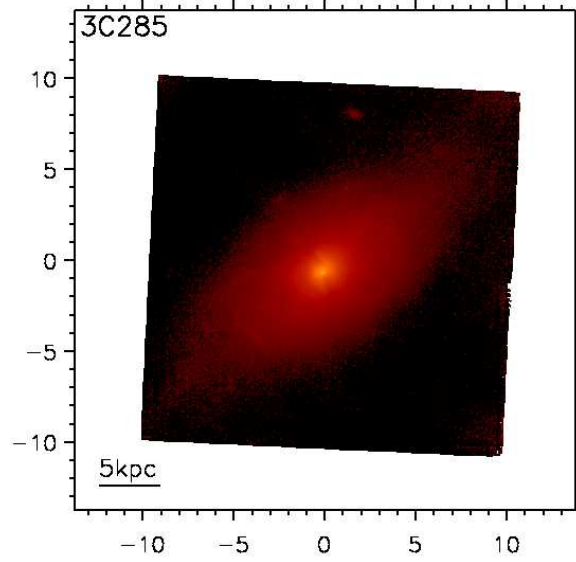


Fig. 43.— HST/NICMOS F160W image of 3C285

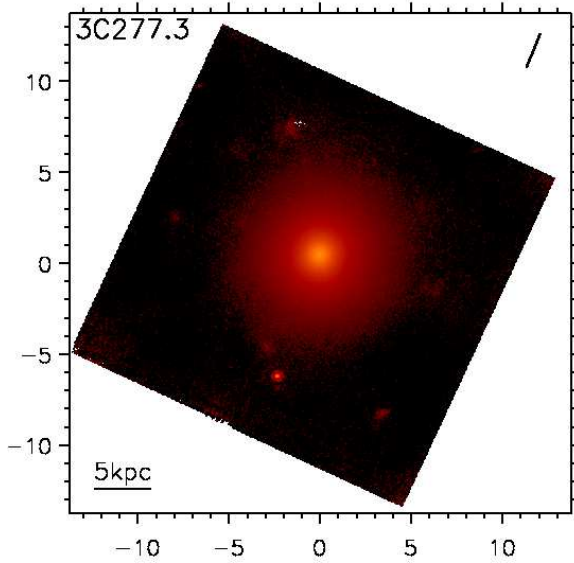


Fig. 42.— HST/NICMOS F160W image of 3C277.3

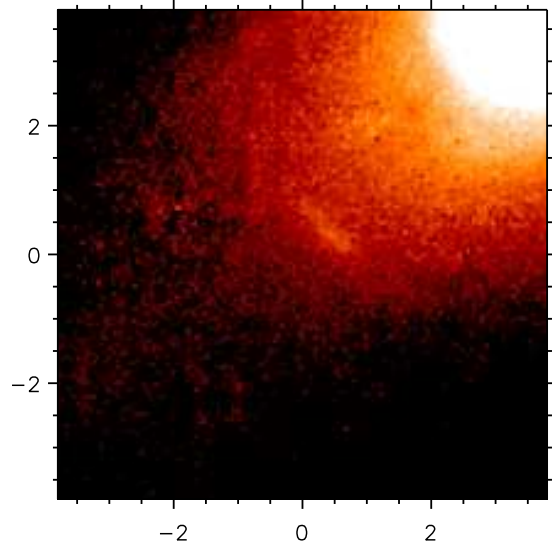


Fig. 44.— Zoom of faint arc-like source south-east of 3C285

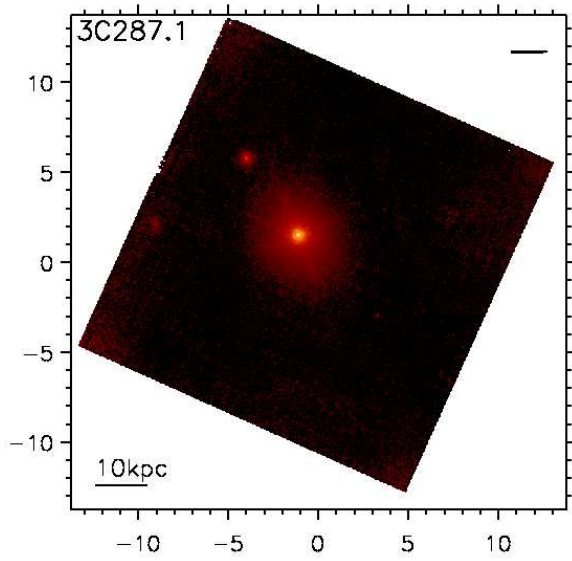


Fig. 45.— HST/NICMOS F160W image of 3C287.1

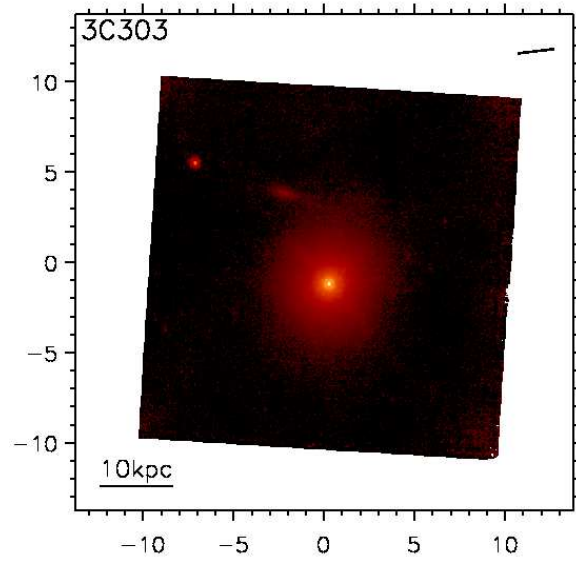


Fig. 47.— HST/NICMOS F160W image of 3C303

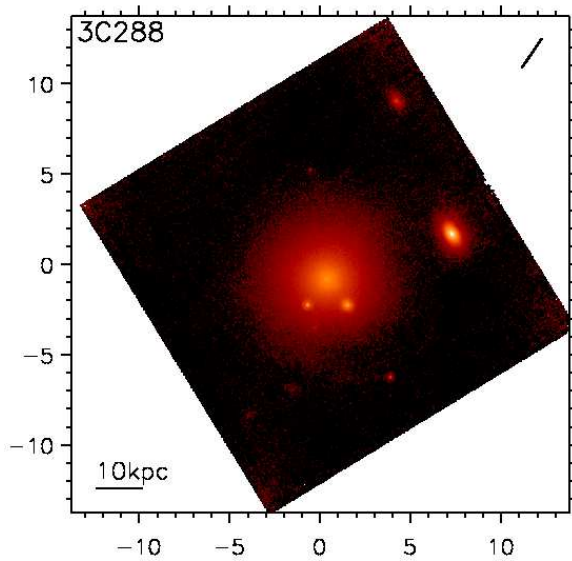


Fig. 46.— HST/NICMOS F160W image of 3C288

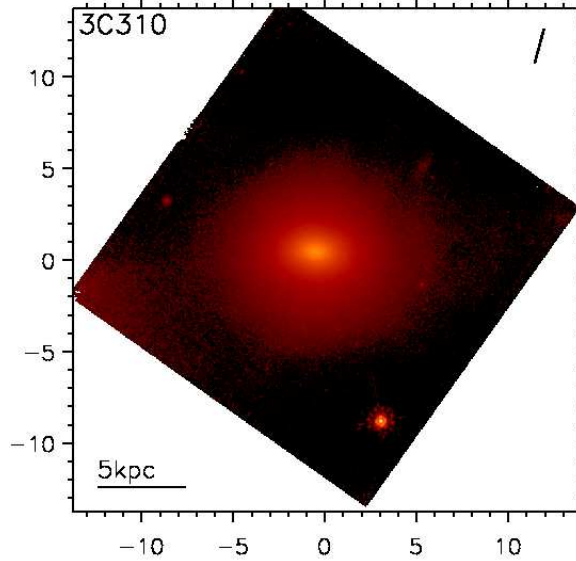


Fig. 48.— HST/NICMOS F160W image of 3C310

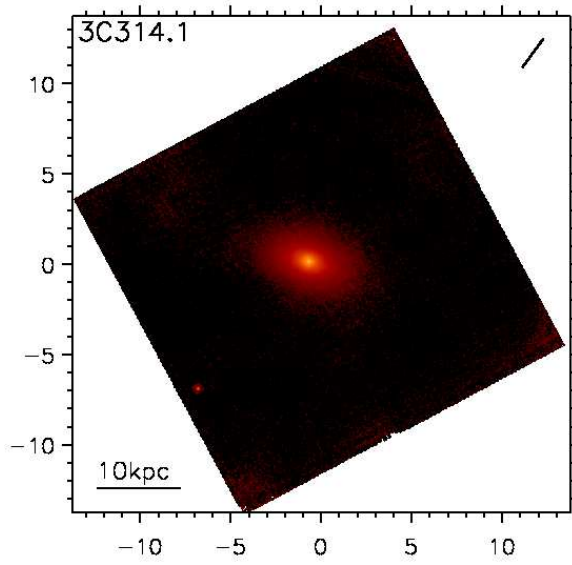


Fig. 49.— HST/NICMOS F160W image of 3C314.1

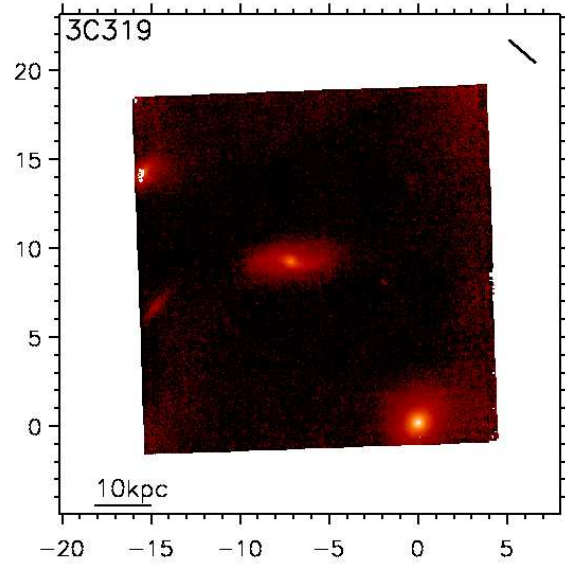


Fig. 51.— HST/NICMOS F160W image of 3C319

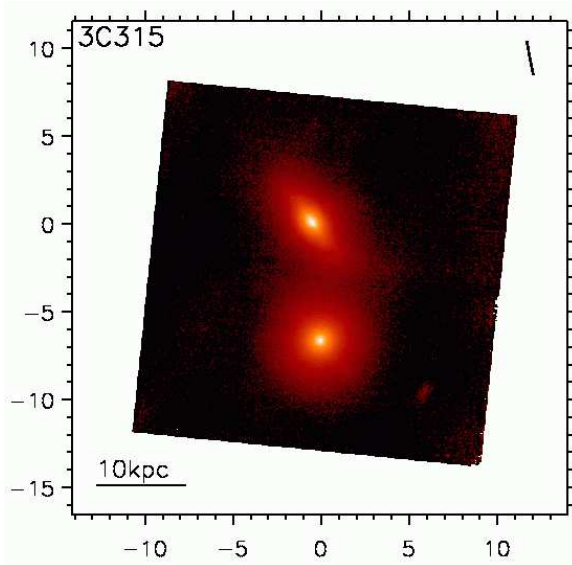


Fig. 50.— HST/NICMOS F160W image of 3C315

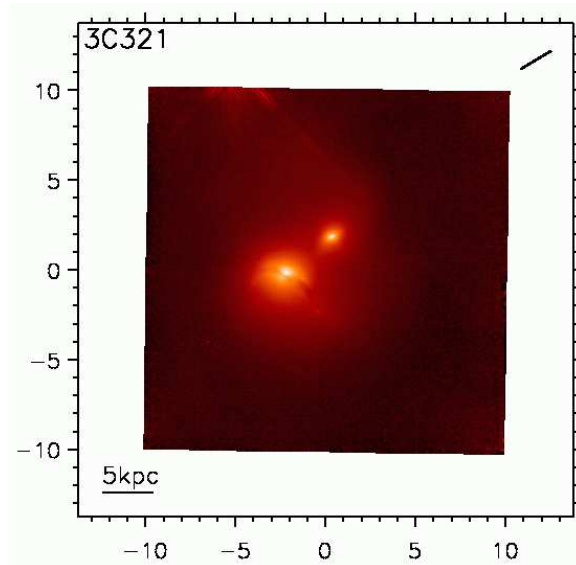


Fig. 52.— HST/NICMOS F160W image of 3C321

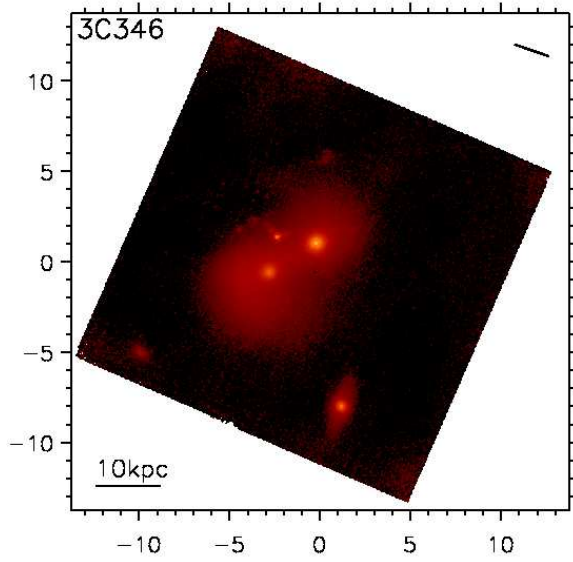


Fig. 53.— HST/NICMOS F160W image of 3C346

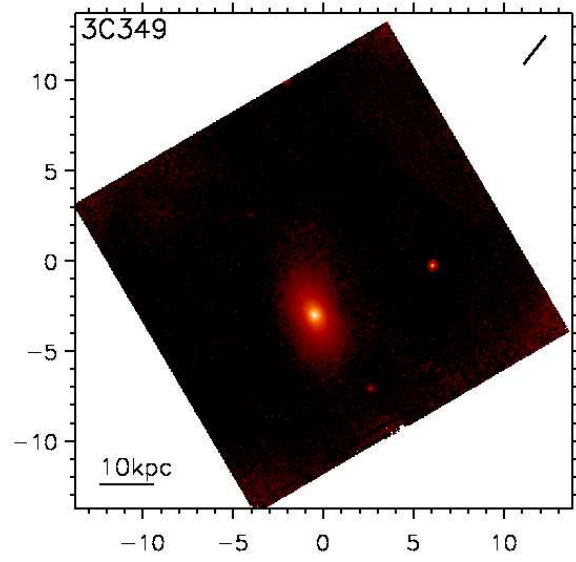


Fig. 55.— HST/NICMOS F160W image of 3C349

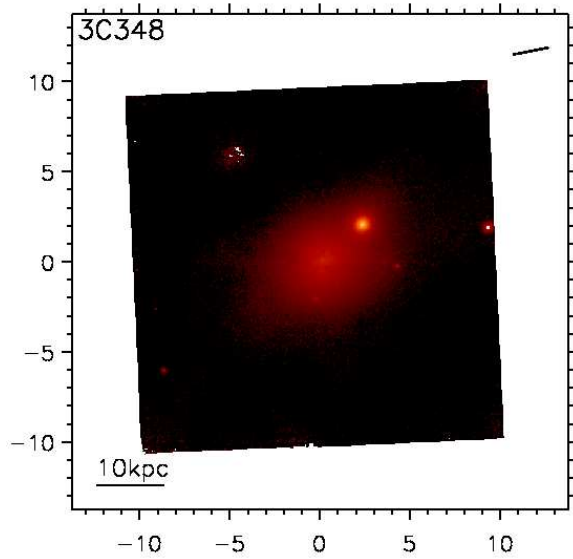


Fig. 54.— HST/NICMOS F160W image of 3C348

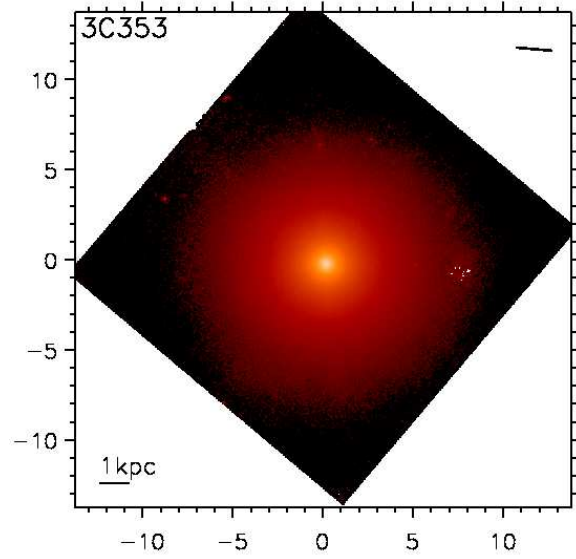


Fig. 56.— HST/NICMOS F160W image of 3C353

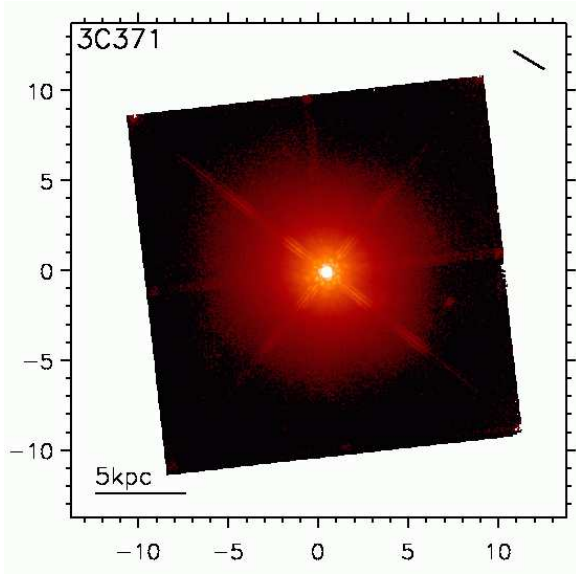


Fig. 57.— HST/NICMOS F160W image of 3C371

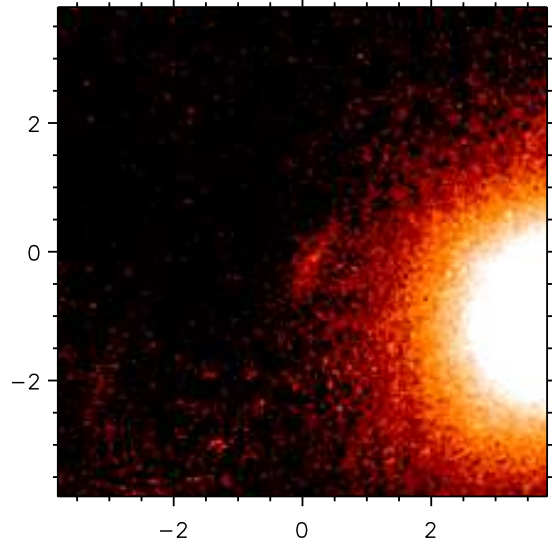


Fig. 59.— Zoom of arc-like feature to the west of 3C379.1

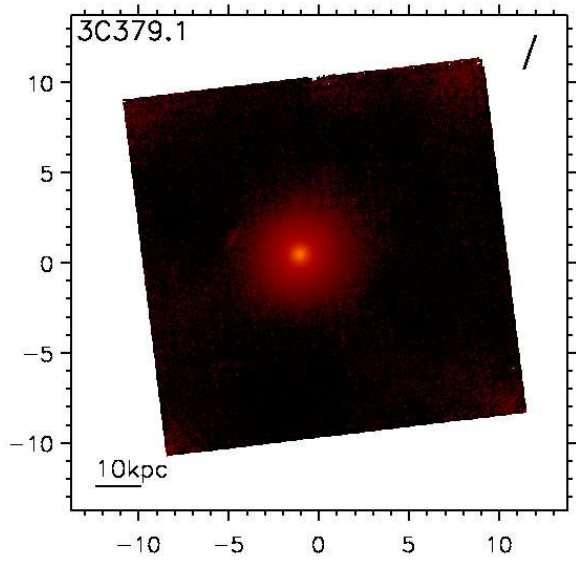


Fig. 58.— HST/NICMOS F160W image of 3C379.1

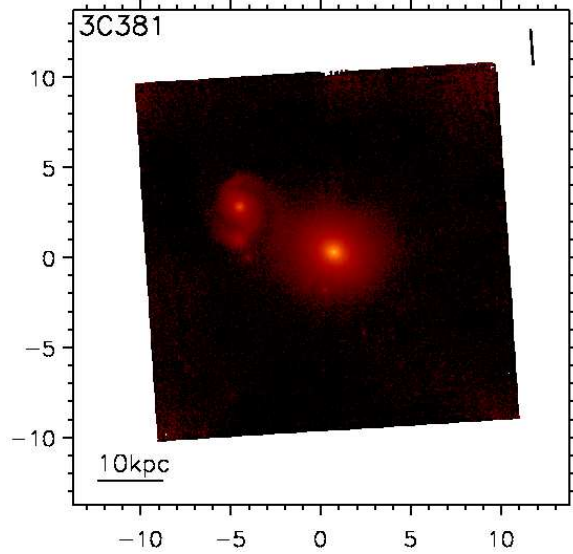


Fig. 60.— HST/NICMOS F160W image of 3C381

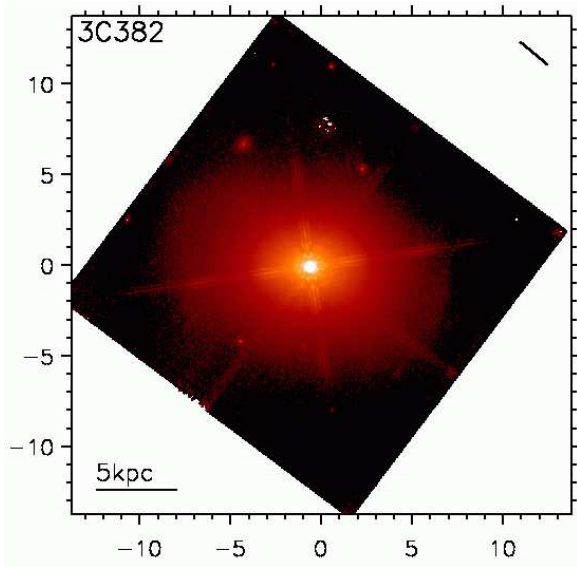


Fig. 61.— HST/NICMOS F160W image of 3C382

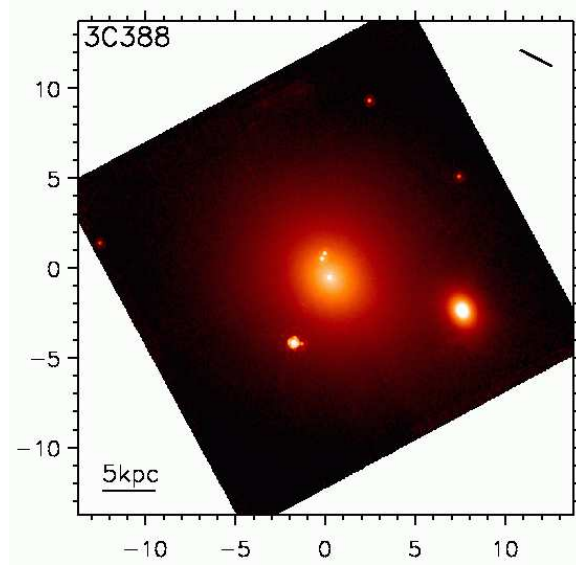


Fig. 63.— HST/NICMOS F160W image of 3C388

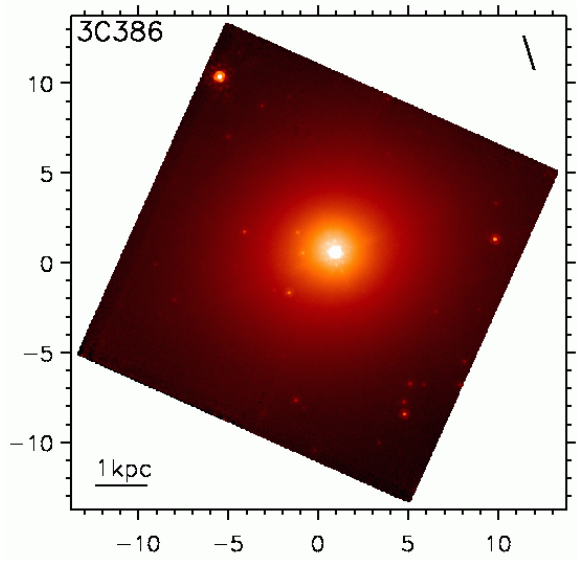


Fig. 62.— HST/NICMOS F160W image of 3C386

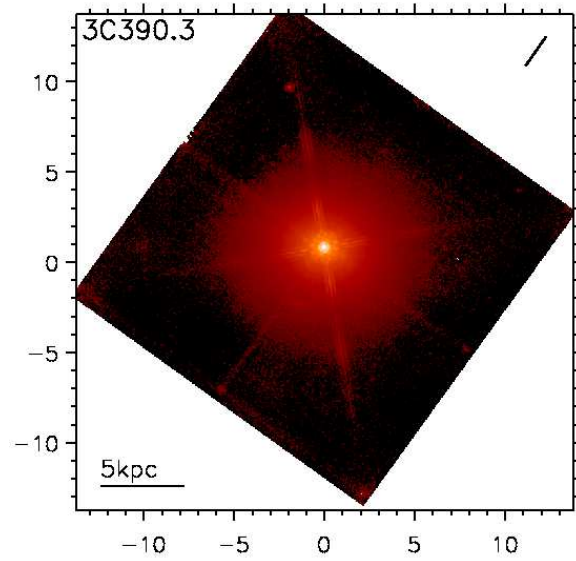


Fig. 64.— HST/NICMOS F160W image of 3C390.3

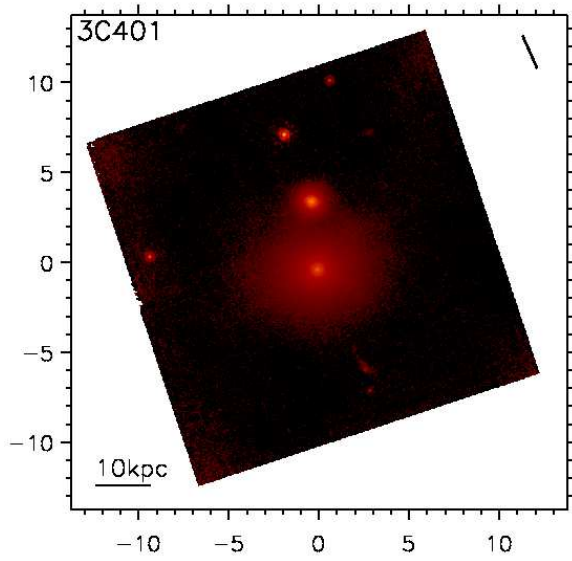


Fig. 65.— HST/NICMOS F160W image of 3C401

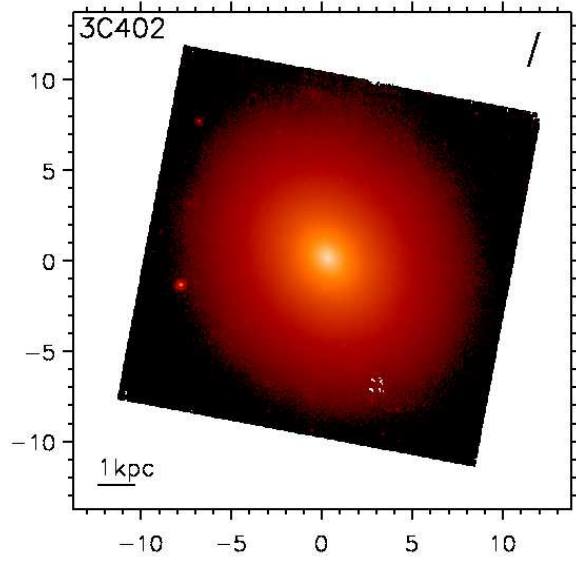


Fig. 67.— HST/NICMOS F160W image of 3C402

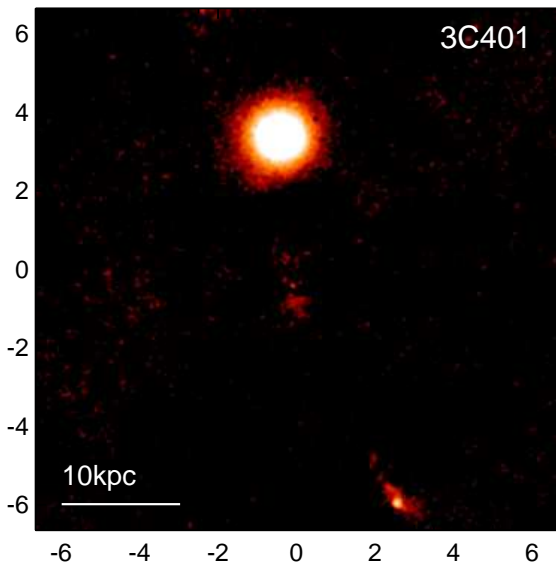


Fig. 66.— Model-subtracted residual for 3C401

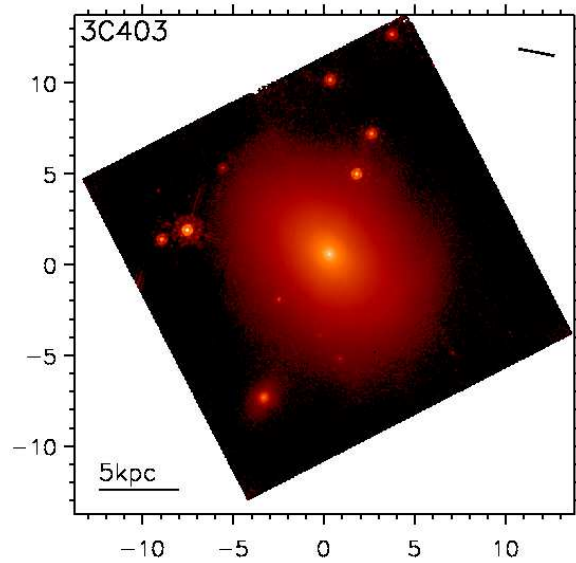


Fig. 68.— HST/NICMOS F160W image of 3C403

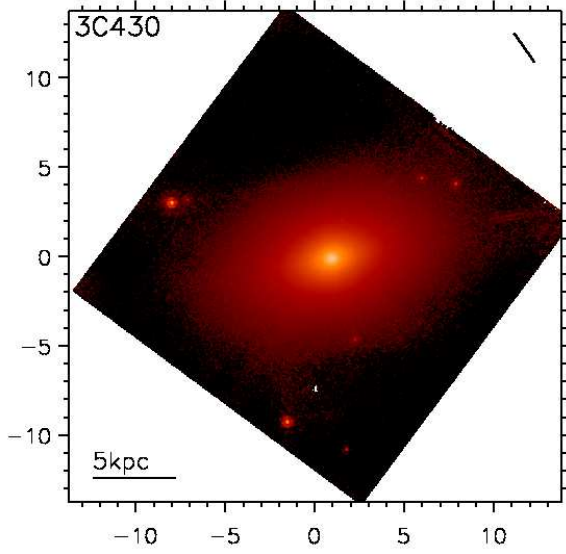


Fig. 69.— HST/NICMOS F160W image of 3C430

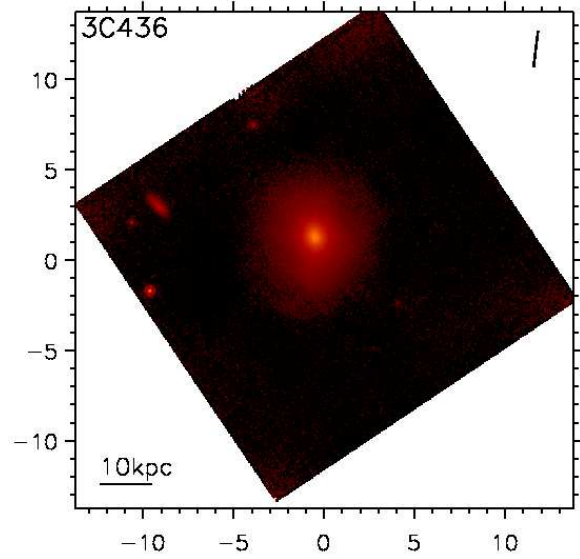


Fig. 71.— HST/NICMOS F160W image of 3C436

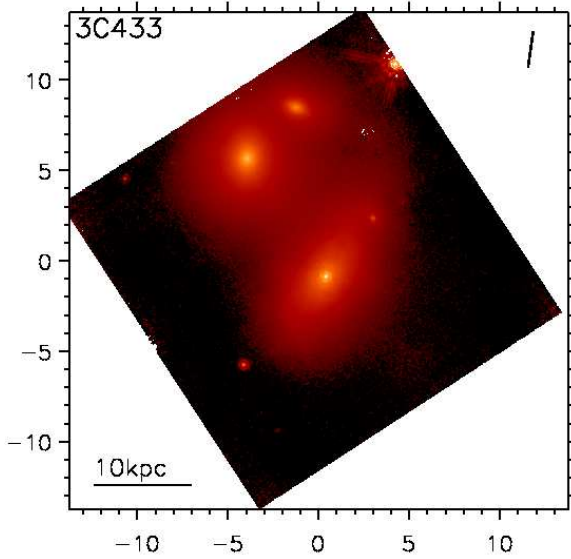


Fig. 70.— HST/NICMOS F160W image of 3C433

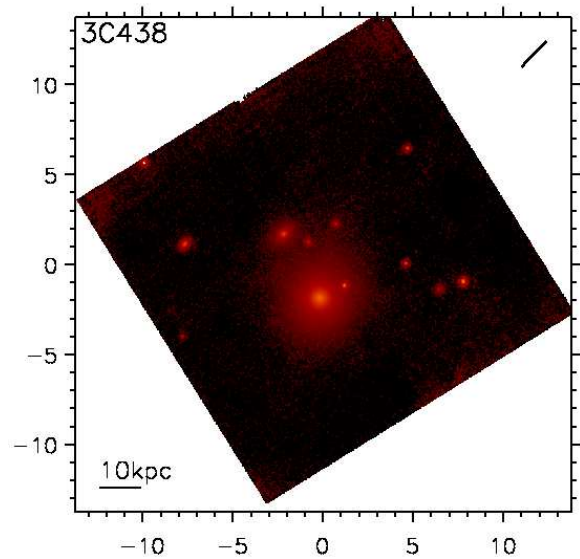


Fig. 72.— HST/NICMOS F160W image of 3C438

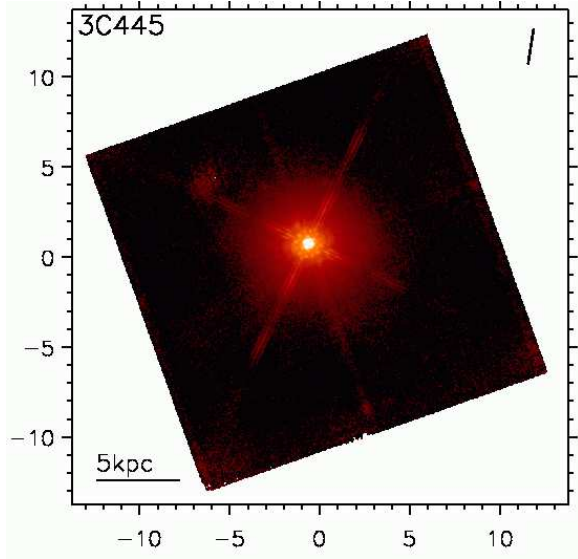


Fig. 73.— HST/NICMOS F160W image of 3C445

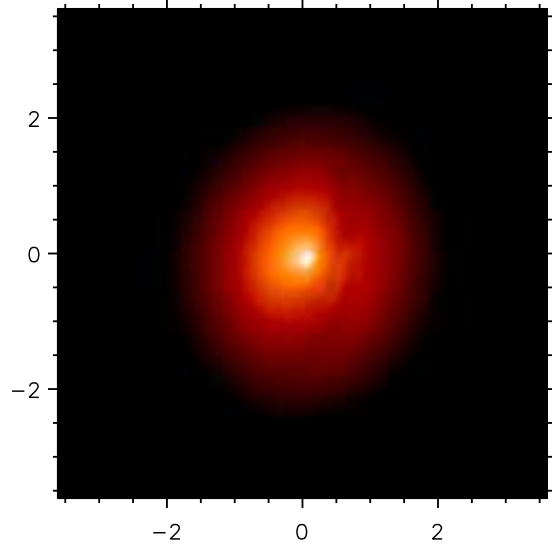


Fig. 75.— Details of the dust lane wrapping around 3C449

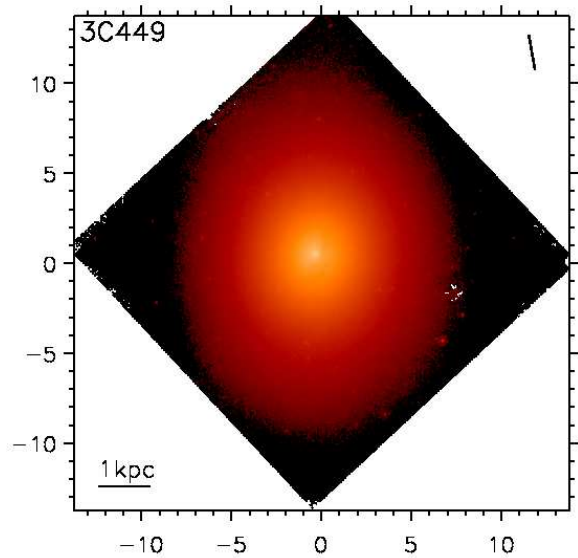


Fig. 74.— HST/NICMOS F160W image of 3C449

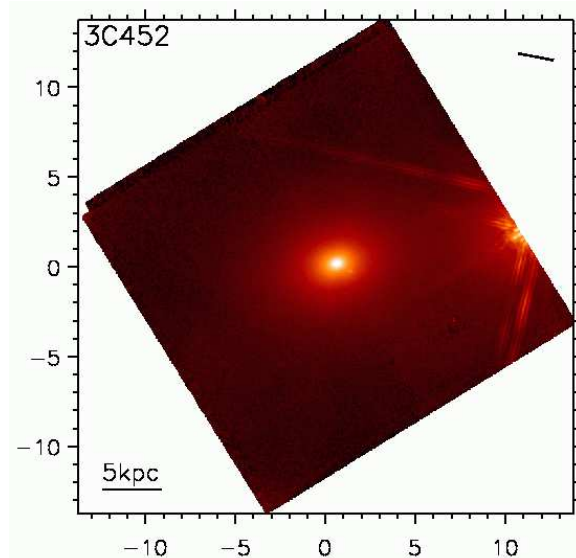


Fig. 76.— HST/NICMOS F160W image of 3C452

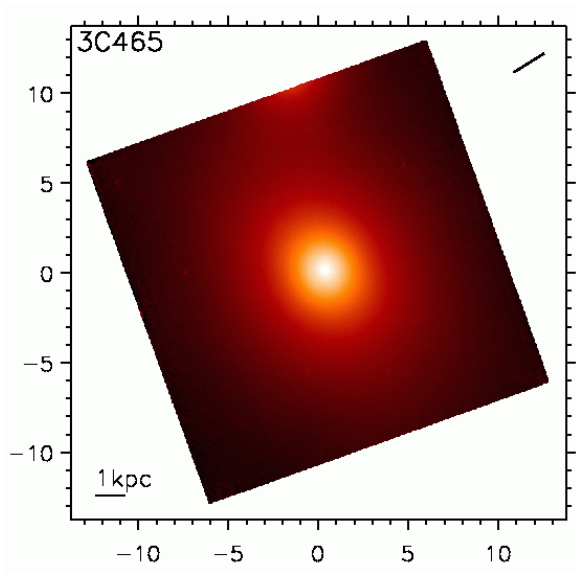


Fig. 77.— HST/NICMOS F160W image of 3C465